Mechanical Systems and Signal Processing 250 (2026) 114146

Contents lists available at ScienceDirect

Mechanical Systems and Signal Processing

journal homepage: www.elsevier.com/locate/ymssp

Full length article

A mixed-norm regularized time-domain inverse framework for localizing and quantifying rotor noise sources

Ying Xu [a,b,c], Zhonghua Peng [a], Damiano Casalino [d], Xiaozheng Zhang [a], Yunjin Tong [e], Chuanxing Bi [a,*], Shiying Xiong [f,*]

[a] Institute of Sound and Vibration Research, Hefei University of Technology, Hefei, Anhui 230009, China
[b] Anhui Province Key Laboratory of Digital Design and Manufacturing, Hefei, Anhui 230009, China
[c] Anhui Feixiang Electric Appliance Co., Cheng Xuan, Anhui 242600, China
[d] Flow Physics and Technology Department, Delft University of Technology, Kluyverweg 1, Delft 2629HS, The Netherlands
[e] Graduate School of Business, Stanford University, Stanford, CA 94305, USA
[f] Department of Engineering Mechanics, School of Aeronautics and Astronautics, Zhejiang University, Hangzhou, Zhejiang 310027, China

ARTICLE INFO

Communicated by E. Fernandez-Grande

Keywords:
Time-domain inverse method
Ffowcs Williams–Hawkings equation
Rotor noise sources
Mixed-norm regularization

ABSTRACT

Conventional source identification methods for rotating machinery are generally formulated in the frequency domain under the assumption of steady or quasi-steady sources, which limits their ability to resolve temporally evolving source behaviour. Time-domain approaches such as the rotating source identifier and virtual rotating arrays allow source localization at individual time instances but are often inadequate for quantifying the evolving strength of unsteady rotating sources. In this study, a time-domain inverse method is developed based on the integral solution of the Ffowcs Williams–Hawkings equation with quadrupole source terms being neglected. An equivalent source model is employed to establish a time-resolved mapping between measured acoustic pressures and source strengths. A mixed-norm regularization scheme is introduced to incorporate prior knowledge of the spatiotemporal characteristics of the source field, enabling stable and accurate reconstruction of time-varying source strengths. The method is validated through numerical simulations over a range of rotational speeds and signal-to-noise ratios, as well as the rotor noise experiments of an unmanned aerial vehicle conducted in a semi-anechoic chamber. The results demonstrate that the method can localize rotor noise sources, capture their temporal evolution, and accurately predict radiated sound fields across a range of operating conditions.

1. Introduction

Rotating machinery, such as rotors, propellers, and wind turbines, is a well-known source of aerodynamic noise due to the complex, unsteady interactions between rotating components and the surrounding flow field [1–4]. Identifying and characterizing such rotating noise sources is essential for both understanding underlying generation mechanisms and designing effective noise mitigation strategies [5–7].

Traditional source identification methods for rotating systems are commonly formulated in the frequency domain and typically assume steady or quasi-steady source behaviour [8–12]. These approaches have yielded useful insights into tonal and broadband radiation mechanisms; however, their applicability is limited in scenarios where source strength and position exhibit significant

* Corresponding authors.
E-mail addresses: cxbi@hfut.edu.cn (C. Bi), shiying.xiong@zju.edu.cn (S. Xiong).

https://doi.org/10.1016/j.ymssp.2026.114146
Received 14 September 2025; Received in revised form 21 February 2026; Accepted 10 March 2026
Available online 17 March 2026

temporal variability due to blade motion, structural deformation, or unsteady inflow conditions [13]. In particular, frequency-domain formulations cannot adequately capture dynamically evolving sound-generation features, especially when multiple physical processes act simultaneously and interact in a time-dependent manner.

Time-domain methods have been introduced to address these limitations. One widely adopted technique is the rotating source identifier (ROSI) [14], which employs delay-and-sum beamforming based on a time-domain propagation model to identify rotating sources from fixed-array measurements. This method has been successfully applied in a range of experimental studies involving helicopters, wind turbines, and engine rotors [15–20]. Despite its robustness, the ROSI method exhibits limited performance when handling high-speed rotation or strong Doppler effects, where increased sidelobe levels can degrade localization accuracy.

Extensions to the ROSI framework include deconvolution techniques and virtual rotating arrays [21,22], which interpolate stationary-array data to emulate a rotating frame [23,24] and thereby enable the use of traditional reconstruction algorithms in a quasi-stationary frame [25,26]. However, these techniques often impose geometric constraints, such as requiring coaxial array-source configurations, and may still struggle with source quantification in the presence of multiple coherent emitters.

Meanwhile, efforts have been made to develop high-resolution source identification methods that integrate computational models with time-resolved experimental data. For example, Casalino et al. [27,28] utilized CLEAN-SC beamforming on pressure signals synthesized in the rotating frame using a frequency-domain Ffowcs Williams–Hawkings (FW–H) formulation, producing broadband noise source maps in rotor simulations. Despite their potential, these methods depend heavily on preprocessing steps to remove motion-induced fluctuations, and their applicability to real-time experimental diagnostics remains limited.

Time-domain inverse methods offer an alternative by establishing a direct relationship between the time histories of source strength and measured acoustic pressures. To address the scattering effects in moving media, Wang et al. compared various numerical methods [29–33] and proposed the convective time-domain equivalent source method to model these effects [34]. Under the assumption of dipole-type radiation, several studies have proposed identification techniques based on simplified formulations of the FW–H equation [35–37], often coupled with spatiotemporal regularization to reconstruct unsteady rotating force distributions. These methods have shown promising results in both numerical and experimental settings, particularly for light and low-speed rotor systems where monopole contributions are negligible.

However, for configurations involving thick blades, high rotational speeds, or elevated freestream velocities, monopole radiation becomes increasingly significant. To account for this, Zhang et al. introduced a time-domain equivalent source method (ESM) based on the monopole assumption and validated through experiments with rotating loudspeakers [38]. Nevertheless, such approaches can face challenges in numerical stability and interpretability, due to the time-varying nature of the source–receiver transfer relationship and the indirect connection between source integrals and physical source strength. Furthermore, it is important to note that for rotating machinery mentioned, such as wind turbines or rotors, aerodynamic loading noise is often non-negligible or even dominant.

In the present study, we extend this work by developing a time-domain inverse method that concurrently accounts for monopole and dipole source mechanisms, which we referred to as mixed-source spatio-temporal time-domain inverse method (MST-TDIM), starting from the FW–H integral solution with quadrupole source terms being neglected. Our approach introduces a physically interpretable mapping between acoustic pressure measurements and equivalent monopole source strengths by using an equivalent source representation. The inversion framework incorporates mixed-norm regularization informed by prior knowledge of the spatiotemporal behaviour of the sources, which enhances robustness in the presence of measurement noise and ill-conditioning.

The proposed formulation aims to achieve not only accurate localization but also time-resolved quantification of rotating source strengths, offering clearer physical insights into source evolution. The methodology is validated through numerical simulations across varying rotation speeds and signal-to-noise ratios, and through the rotor noise experiments of an unmanned aerial vehicle conducted in a semi-anechoic chamber. These results demonstrate the feasibility of the approach for real-time acoustic diagnostics of rotating systems, and lay the foundation for future applications in aeroacoustic design and control.

The remainder of the paper is organized as follows. In Section 2, the governing equations are derived from the integral formulation of the FW–H equation with quadrupole source terms being neglected, and a time-domain inverse model is constructed based on an equivalent source representation. The mixed-norm regularization framework used to stabilize the inversion is also introduced. Section 3 presents numerical evaluations involving rotating monopole and dipole sources under varying rotational speeds and signal-to-noise ratios , as thickness noise and loading noise constitute the dominant sources of subsonic rotor noise. The method's performance is assessed in terms of source strength reconstruction, spatial localization, and far-field sound prediction. Section 4 presents experimental results from rotor noise of an unmanned aerial vehicle in a semi-anechoic chamber, validating the method under controlled but realistic acoustic conditions. Section 5 concludes the paper by summarizing the key findings and discusses future directions, including the extension of the framework to supersonic regimes and the treatment of more complex source dynamics.

2. Theoretical foundation

2.1. Aeroacoustic framework

Predicting sound generated by unsteady, compressible flows in the presence of solid boundaries remains a foundational problem in aeroacoustics. Lighthill's acoustic analogy [39] reformulates the compressible Navier–Stokes (NS) equations into a wave equation, enabling the study of aerodynamic noise as a perturbation problem. The FW–H equation [40] extends this framework to incorporate arbitrary boundary motion, thus providing a general method for sound prediction in configurations involving complex geometries and moving surfaces.

The compressible NS equations in Cartesian coordinates describe the conservation of mass and momentum in a viscous fluid [41]:

$$\begin{cases} \frac{\partial \rho}{\partial t} + \frac{\partial(\rho u_j)}{\partial x_j} = 0, \\ \frac{\partial(\rho u_i)}{\partial t} + \frac{\partial(\rho u_i u_j + p_{ij})}{\partial x_j} = 0, \end{cases} \tag{1}$$

where ρ is the density and u_i are the fluid velocity components. The stress tensor, $p_{ij} = p\delta_{ij} - \tau_{ij}$, consists of the pressure term p and the viscous stress tensor τ_{ij}, which is defined as $\tau_{ij} = \mu(\partial u_i/\partial x_j + \partial u_j/\partial x_i - (2/3)(\partial u_k/\partial x_k)\delta_{ij})$, with μ representing the dynamic viscosity.

Assuming a quiescent background medium of constant density ρ_0 and sound speed c_0, Lighthill [39] derived the inhomogeneous wave equation for the density perturbation $\rho' = \rho - \rho_0$:

$$\left(\frac{\partial^2}{\partial t^2} - c_0^2 \nabla^2\right) \rho' = \frac{\partial^2 T_{ij}}{\partial x_i \partial x_j}, \tag{2}$$

where the Lighthill stress tensor is defined as $T_{ij} = \rho u_i u_j + (p - c_0^2 \rho)\delta_{ij} - \tau_{ij}$. The speed of sound c_0 is related to the isentropic compressibility of the medium by $c_0^2 = (\partial p/\partial \rho)_s$, where the derivative is taken at constant entropy s, reflecting the assumption of small, adiabatic, and reversible perturbations. Under these conditions, the pressure fluctuation is approximated by:

$$p' = c_0^2 \rho'. \tag{3}$$

Eq. (2) characterizes wave propagation in a homogeneous, unbounded medium and does not incorporate the effects of solid boundaries. To address this limitation, Ffowcs Williams and Hawkings [42] proposed a surface-based formulation utilizing generalized functions. Let $f(\boldsymbol{x}, t) = 0$ define a time-dependent surface enclosing the acoustic sources. To eliminate ambiguity, we assume that f is a signed distance function, which ensures a unique value at each point $(\boldsymbol{x}, t)$ and satisfies the eikonal equation $|\boldsymbol{\nabla} f| = 1$. The Heaviside function $H(f)$ and the Dirac delta function $\delta(f)$ then serve to partition the domain into volume and surface contributions, respectively.

Applying the wave operator to $\rho' H(f)$ and using distributional calculus and in conjunction with Eq. (3), the FW–H equation takes the form:

$$\left(\frac{1}{c_0^2}\frac{\partial^2}{\partial t^2} - \nabla^2\right)[p' H(f)] = \frac{\partial^2}{\partial x_i \partial x_j}\left[T_{ij} H(f)\right] - \frac{\partial}{\partial x_i}\left[F_i \delta(f)\right] + \frac{\partial}{\partial t}\left[q\delta(f)\right], \tag{4}$$

where the surface source terms are $F_i = [\rho u_i(u_j - v_j) + p_{ij}]n_j$ and $q = (\rho u_j - \rho' v_j)n_j$, respectively. Here, v_i is the velocity of the moving surface, and n_i is the outward normal vector to the surface $f = 0$.

Acoustic sources may be classified, in a multipole sense [43], into monopoles, dipoles and quadrupoles. The monopole represents a net volumetric source, such as mass injection or displacement; the dipole corresponds to an unsteady force acting on the fluid; and the quadrupole arises from the interaction of fluctuating stresses. In this context, Eq. (4) extends Lighthill's analogy by incorporating all three source mechanisms: q, representing monopole contributions due to volumetric changes; F_i, capturing dipole effects from surface loading; and T_{ij}, describing quadrupole sources originating from turbulence. This formulation thus provides a unified representation of sound generation in flows involving both turbulence and moving boundaries.

2.2. Integral solution of FW-H equation

The FW–H equation, given in Eq. (4), provides a generalized framework for predicting sound radiation from unsteady, compressible flows in the presence of arbitrarily moving surfaces [42]. In many aeroacoustic applications of practical relevance, particularly those involving rotating machinery operating at low Mach numbers such as axial cooling fans or marine propellers, the radiated sound may arise from a combination of monopole and dipole mechanisms, and in some configurations the dipole contribution can even become dominant. The monopole source is represented by the time derivative $\partial[q\delta(f)]/\partial t$ in Eq. (4), and accounts for volumetric displacement effects associated with the motion of the surface. The dipole source is represented by the divergence term $-\partial[F_i\,\delta(f)]/\partial x_i$, and describes sound generation due to unsteady aerodynamic loading, including fluctuating surface pressure and shear stresses on the control surface, providing a more complete representation of the rotor acoustic field. The governing equation for the rotor acoustic pressure perturbation is given by:

$$\left(\frac{1}{c_0^2}\frac{\partial^2}{\partial t^2} - \nabla^2\right)\left[p' H(f)\right] = \frac{\partial}{\partial t}\left[q(\boldsymbol{y}, t)\,\delta\big(f(\boldsymbol{y}, t)\big)\right] - \frac{\partial}{\partial x_i}\left[F_i(\boldsymbol{y}, t)\,\delta\big(f(\boldsymbol{y}, t)\big)\right], \tag{5}$$

where $H(f)$ is the Heaviside function associated with the exterior of the moving surface, and $f(\boldsymbol{y}, t) = 0$ implicitly defines the surface location in spacetime.

The solution to Eq. (5) is obtained using the Green's function corresponding to the free-space wave operator. The fundamental solution $G(\boldsymbol{x}, t; \boldsymbol{y}, \tau)$ satisfies

$$\left(\frac{1}{c_0^2}\frac{\partial^2}{\partial t^2} - \nabla^2\right) G(\boldsymbol{x}, t; \boldsymbol{y}, \tau) = \delta(\boldsymbol{x} - \boldsymbol{y})\,\delta(t - \tau), \tag{6}$$

and takes the form

$$G(\boldsymbol{x}, t; \boldsymbol{y}, \tau) = \frac{1}{4\pi R}\,\delta\left(t - \tau - \frac{R}{c_0}\right), \quad \text{with} \quad R = |\boldsymbol{x} - \boldsymbol{y}|, \tag{7}$$

where R denotes the Euclidean distance between the field point $\boldsymbol{x}$ and the source point $\boldsymbol{y}$.

Substituting the Green's function into the formal integral solution yields the following representation:

$$p'(x,t)H(f) = \int_{-\infty}^{+\infty}\int_{\mathbb{R}^3} G(\boldsymbol{x},t;\boldsymbol{y},\tau)\left[\frac{\partial}{\partial\tau}\left\{q(\boldsymbol{y},\tau)\,\delta\big[f(\boldsymbol{y},\tau)\big]\right\} - \frac{\partial}{\partial x_i}\left\{F_i(\boldsymbol{y},\tau)\,\delta\big[f(\boldsymbol{y},\tau)\big]\right\}\right] d\Omega\, d\tau, \tag{8}$$

where $\mathrm{d}\Omega$ denotes the volume element in three-dimensional space. The function $f(\boldsymbol{y},\tau)$ implicitly defines the moving surface $S(\tau)$, such that the zero level set $f(\boldsymbol{y},\tau)=0$ identifies its instantaneous location at emission time τ. The Dirac delta function enforces this condition within the integration, effectively reducing the volume integral over $\mathbb{R}^3$ to a surface integral over $S(\tau)$ that evolves with time.

To facilitate analytical development of the integral representation in Eq. (8), integrations by parts are performed with respect to both the temporal variable τ and the spatial variable $\boldsymbol{y}$. These operations are justified under the standard assumption that the products $q(\boldsymbol{y},\tau)\,G(\boldsymbol{x},t;\boldsymbol{y},\tau)\,\delta[f(\boldsymbol{y},\tau)]$ and $F_i(\boldsymbol{y},\tau)\,G(\boldsymbol{x},t;\boldsymbol{y},\tau)\ \delta[f(\boldsymbol{y},\tau)]$ vanish sufficiently rapidly as $\tau\to\pm\infty$ and on the boundary of the spatial integration domain, such that boundary contributions may be neglected. Applying the temporal distribution identity,

$$\int_{-\infty}^{+\infty} G\,\partial\left[q\,\delta(f)\right]/\partial\tau\,\mathrm{d}\tau = -\int_{-\infty}^{+\infty}(\partial G/\partial\tau)\,q\,\delta(f)\,\mathrm{d}\tau,$$

and similarly, by integration by parts with respect to the spatial variable y_i, $\int_{\mathbb{R}^3} G\,\partial\left[F_i\,\delta(f)\right]/\partial y_i\,\mathrm{d}\Omega = -\int_{\mathbb{R}^3}(\partial G/\partial y_i)\,F_i\,\delta(f)\,\mathrm{d}\Omega$, transforms the integrals into the following alternative expression

$$p'(\boldsymbol{x},t)H(f) = -\int_{-\infty}^{+\infty}\int_{\mathbb{R}^3}\left[\frac{\partial G(\boldsymbol{x},t;\boldsymbol{y},\tau)}{\partial\tau}\,q(\boldsymbol{y},\tau) - \frac{\partial G(\boldsymbol{x},t;\boldsymbol{y},\tau)}{\partial y_i}\,F_i(\boldsymbol{y},\tau)\right]\delta[f(\boldsymbol{y},\tau)]\,\mathrm{d}\Omega\,\mathrm{d}\tau. \tag{9}$$

This formulation is advantageous in the subsequent transformation of the spatial volume integral into a surface integral, by allowing the application of distributional identities for delta functions supported on moving manifolds in space–time.

When the function $f(\boldsymbol{y},\tau)$ is selected to be a signed distance function, it satisfies $|\nabla f(\boldsymbol{y},\tau)| = 1$ by definition. This ensures that the surface is well-defined and uniquely described at each instant in space and time. Applying the standard identity for the Dirac delta function supported on a time-dependent surface, the volume integral over $\mathbb{R}^3$ may be converted into a surface integral over the instantaneous surface $S(\tau)$, which is implicitly defined by the zero level set condition $f(\boldsymbol{y},\tau)=0$. Specifically, we write $S(\tau)=\left\{\boldsymbol{y}\in\mathbb{R}^3 \;\middle|\; f(\boldsymbol{y},\tau)=0\right\}$. Given that $|\nabla f|=1$, the transformation reduces the integration to:

$$p'(\boldsymbol{x},t)\,H(f) = \int_{-\infty}^{+\infty}\int_{S(\tau)}\left[-\frac{\partial G(\boldsymbol{x},t;\boldsymbol{y},\tau)}{\partial\tau}\,q(\boldsymbol{y},\tau) + \frac{\partial G(\boldsymbol{x},t;\boldsymbol{y},\tau)}{\partial y_i}\,F_i(\boldsymbol{y},\tau)\right]\mathrm{d}S\,\mathrm{d}\tau. \tag{10}$$

This formulation allows the time-dependent geometry of the moving surface to be treated within a fixed spatial domain, thereby recasting volumetric integrals as surface integrals that evolve in time.

Substituting the explicit form of the Green's function, given in Eq. (7), into Eq. (10):

$$\frac{\partial G}{\partial\tau} = -\frac{1}{4\pi R}\frac{\partial}{\partial t}\delta\left(t-\tau-\frac{R}{c_0}\right), \tag{11}$$

$$\frac{\partial G}{\partial y_i} = \frac{\tilde{\boldsymbol{R}}}{4\pi}\left[\frac{1}{R^2}\delta\left(t-\tau-\frac{R}{c_0}\right) + \frac{1}{c_0 R}\frac{\partial}{\partial t}\delta\left(t-\tau-\frac{R}{c_0}\right)\right], \tag{12}$$

where $\tilde{\boldsymbol{R}} = (\boldsymbol{x}-\boldsymbol{y})/R$ and we obtain:

$$\begin{aligned} p'(x,t)H(f) = {} & \frac{1}{4\pi}\frac{\partial}{\partial t}\int_{-\infty}^{\infty}\int_{S(\tau)}\frac{q(y,\tau)}{R}\,\delta\left(t-\tau-\frac{R}{c_0}\right)dS\,d\tau \\ & + \frac{1}{4\pi}\int_{-\infty}^{\infty}\int_{S(\tau)}\frac{F_i(y,\tau)\,\tilde{R}_i}{R^2}\,\delta\left(t-\tau-\frac{R}{c_0}\right)dS\,d\tau \\ & + \frac{1}{4\pi c_0}\frac{\partial}{\partial t}\int_{-\infty}^{\infty}\int_{S(\tau)}\frac{F_i(y,\tau)\,\tilde{R}_i}{R}\,\delta\left(t-\tau-\frac{R}{c_0}\right)dS\,d\tau. \end{aligned} \tag{13}$$

To evaluate the delta function in Eq. (13), we define:

$$g_t(\tau) \equiv t-\tau-\frac{|\boldsymbol{x}-\boldsymbol{y}(\tau)|}{c_0}, \tag{14}$$

whose root $\tau=\tau_e$ corresponds to the retarded time. Then, using the standard identity for delta functions $\delta(g_t(\tau)) = \delta(\tau-\tau_e)/|\partial g_t/\partial\tau|_{\tau=\tau_e}$, with

$$\frac{\partial g_t}{\partial\tau} = 1-\boldsymbol{M}\cdot\tilde{\boldsymbol{R}} = 1-M_R, \tag{15}$$

where $\boldsymbol{M} = \mathrm{d}\boldsymbol{y}/(c_0 \mathrm{d}\tau)$ is the local Mach vector. Inserting this into Eq. (13), the integral becomes

$$\begin{aligned} & p'(x,t)H(f) \\ =& \frac{1}{4\pi}\frac{\partial}{\partial t}\int_{S(\tau_e)} \frac{q(y,\tau_e)}{R(1-M_R)}\,dS \\ &+ \frac{1}{4\pi}\int_{S(\tau_e)} \frac{F_i(y,\tau_e)\tilde{R}_i}{R^2(1-M_R)}\,dS + \frac{1}{4\pi c_0}\frac{\partial}{\partial t}\int_{S(\tau_e)} \frac{F_i(y,\tau_e)\tilde{R}_i}{R(1-M_R)}\,dS. \end{aligned} \tag{16}$$

In the evaluation of expression, given in Eq. (16), it is convenient to first note that the observer location $\boldsymbol{x}$ is assumed to lie in the exterior acoustic domain, outside the moving surface defined by $f(\boldsymbol{y},\tau) = 0$. As a result, the Heaviside function $H(f)$ is identically unity throughout the region of interest, and may therefore be omitted from subsequent formulations of the acoustic pressure.

To proceed analytically, the surface integral in Eq. (16) is projected onto a fixed spatial surface S, whereby the source position $\boldsymbol{y}$ is expressed explicitly as a function of the retarded time τ, in accordance with the radiation condition $|\boldsymbol{x} - \boldsymbol{y}(\tau)| = c(t-\tau)$ [43]. This change of variables permits the interchange of the temporal derivative and surface integration. By applying the chain-rule identity given in Eq. (15), the integral may then be recast as a time derivative evaluated on the surface S. Specifically, this yields

$$\begin{aligned} & p'(\boldsymbol{x},t) \\ =& \frac{1}{4\pi}\int_S \left\{ \frac{\dot{q}}{R(1-M_R)^2} - \frac{q}{R^2(1-M_R)^2}\frac{\partial R}{\partial \tau} + \frac{q}{R(1-M_R)^3}\frac{\partial M_R}{\partial \tau} \right\}_{\tau=\tau_e} \mathrm{d}S \\ &+ \frac{1}{4\pi c_0}\int_S \left\{ \frac{\dot{F}_i\tilde{R}_i + F_i\dot{\tilde{R}}_i}{R(1-M_R)^2} \right\}_{\tau=\tau_e} \mathrm{d}S - \frac{1}{4\pi c_0}\int_S \left\{ \frac{\partial R}{\partial \tau}\frac{F_i\tilde{R}_i}{R^2(1-M_R)^2} \right\}_{\tau=\tau_e} \mathrm{d}S \\ &+ \frac{1}{4\pi c_0}\int_S \left\{ \frac{\partial M_R}{\partial \tau}\frac{F_i\tilde{R}_i}{R(1-M_R)^3} \right\}_{\tau=\tau_e} \mathrm{d}S + \frac{1}{4\pi}\int_S \left\{ \frac{F_i\tilde{R}_i}{R^2(1-M_R)} \right\}_{\tau=\tau_e} \mathrm{d}S, \end{aligned} \tag{17}$$

where $\dot{q} = \partial q/\partial\tau$ and $\dot{F}_i = \partial F_i/\partial\tau$ denotes the local time derivative of the source term. The required time derivatives of the geometric and kinematic quantities are given by:

$$\frac{\partial R}{\partial \tau} = -c_0 M_R, \tag{18}$$

and

$$\begin{aligned} \frac{\partial M_R}{\partial \tau} &= \frac{\partial \boldsymbol{M}}{\partial \tau}\cdot\tilde{\boldsymbol{R}} + \boldsymbol{M}\cdot\frac{\partial \tilde{\boldsymbol{R}}}{\partial \tau} \\ &= \dot{\boldsymbol{M}}\cdot\tilde{\boldsymbol{R}} + \boldsymbol{M}\cdot\left[\frac{c_0 R(\boldsymbol{M} - M_R\tilde{\boldsymbol{R}})}{R^2}\right] \\ &= \dot{\boldsymbol{M}}\cdot\tilde{\boldsymbol{R}} - \frac{c_0}{R}\left(|\boldsymbol{M}|^2 - M_R^2\right). \end{aligned} \tag{19}$$

Substituting Eqs. (18) and (19) into the expression for $p'(\boldsymbol{x},t)$ yields the compact form

$$\begin{aligned} p'(\boldsymbol{x},t) = \frac{1}{4\pi}\int_S \Bigg[& \frac{\dot{q}}{R(1-M_R)^2} + \frac{\dot{\boldsymbol{M}}\cdot\tilde{\boldsymbol{R}}\,q}{R(1-M_R)^3} + \frac{c_0(M_R - |\boldsymbol{M}|^2)\,q}{R^2(1-M_R)^3} \\ & + \frac{1}{c_0}\frac{\dot{F}_i\tilde{R}_i}{R(1-M_R)^2} - \frac{M_i F_i}{R^2(1-M_R)^2} + \frac{1}{c_0}\frac{(\dot{\boldsymbol{M}}\cdot\tilde{\boldsymbol{R}})(F_i\tilde{R}_i)}{R(1-M_R)^3} \\ & + \frac{(1-|\boldsymbol{M}|^2)(F_i\tilde{R}_i)}{R^2(1-M_R)^3} \Bigg]_{\tau=\tau_e} \mathrm{d}S, \end{aligned} \tag{20}$$

which describes the acoustic pressure radiated by combined time-dependent monopole and dipole source distributions convected by a moving surface. The first term captures the local temporal variation of the source, while the second and third terms arise from convective effects due to the source motion relative to the observer. The remaining terms represent the dipole contribution, describing sound radiation due to unsteady aerodynamic loading on the surface. The first dipole term is associated with the local temporal variation of the loading, the second term reflects convection of the loading by the moving surface, and the last two terms arise from acceleration and convective amplification effects.

2.3. Time-domain inversion for rotating acoustic sources

The surface integral in Eq. (20) is generally intractable in closed form due to the geometric complexity of the source region and the dependence on retarded time. For numerical implementation, the continuous distribution of monopole and dipole sources are replaced by a finite set of discrete sources [44], which transforms the integral formulation into a linear system of equations [45]. The aim of the inverse procedure is to estimate a vector of source strengths that best fits the measured acoustic pressure in a least-squares sense. To this end, the blade planform is discretized into N equivalent source locations, as shown in Fig. 1. These locations, indicated by solid circles, define the spatial support of the equivalent monopole sources and dipole sources and provide the framework for constructing the forward and inverse models.

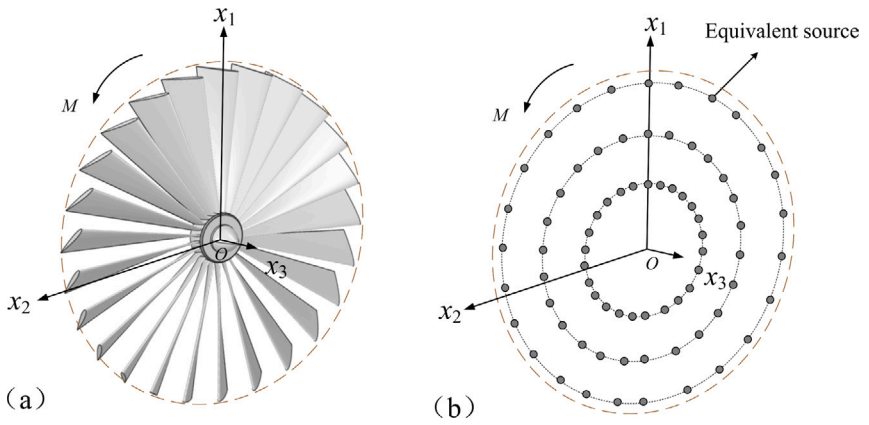

Fig. 1. (a) Geometric description of the rotor planform showing the rotating blades, with x_1, x_2, and x_3 denoting the coordinate axes and M the rotational Mach number. (b) Equivalent discrete source representation of the rotor surface, where the continuous monopole source distribution is replaced by N equivalent point sources (solid circles) arranged on concentric rings around the hub. These equivalent sources form the spatial basis for constructing the forward acoustic model and for estimating source strengths in the inverse problem.

In the present formulation, the sound field produced by rotating sources is represented by a distribution of N equivalent sources, each located at a prescribed position on the discretized source surface. Upon discretizing the surface integrals in Eq. (20), a linear relationship is established between the time-dependent strengths of the equivalent sources and the resulting acoustic pressure at the observer location. The discretized expression for the radiated pressure field takes the form

$$\begin{aligned} p'(\boldsymbol{x},t) = \frac{1}{4\pi}\Bigg\{ & \sum_{n=1}^{N}\left[\frac{\dot{q}_n}{R_n\left(1-\boldsymbol{M}_n\cdot\tilde{\boldsymbol{R}}_n\right)^2}\right] + \sum_{n=1}^{N}\left[\frac{\dot{\boldsymbol{M}}_n\cdot\tilde{\boldsymbol{R}}_n\, q_n}{R_n\left(1-\boldsymbol{M}_n\cdot\tilde{\boldsymbol{R}}_n\right)^3}\right] \\ & + \sum_{n=1}^{N}\left[\frac{c_0\left(\boldsymbol{M}_n\cdot\tilde{\boldsymbol{R}}_n-|\boldsymbol{M}_n|^2\right)q_n}{R_n^2\left(1-\boldsymbol{M}_n\cdot\tilde{\boldsymbol{R}}_n\right)^3}\right] + \sum_{n=1}^{N}\left[\frac{1}{c_0}\,\frac{\dot{F}_{ni}\,\tilde{R}_{ni}}{R_n\left(1-\boldsymbol{M}_n\cdot\tilde{\boldsymbol{R}}_n\right)^2}\right] \\ & - \sum_{n=1}^{N}\left[\frac{M_{ni}\,F_{ni}}{R_n^2\left(1-\boldsymbol{M}_n\cdot\tilde{\boldsymbol{R}}_n\right)^2}\right] + \sum_{n=1}^{N}\left[\frac{1}{c_0}\,\frac{\left(\dot{\boldsymbol{M}}_n\cdot\tilde{\boldsymbol{R}}_n\right)\left(F_{ni}\tilde{R}_{ni}\right)}{R_n\left(1-\boldsymbol{M}_n\cdot\tilde{\boldsymbol{R}}_n\right)^3}\right] \\ & + \sum_{n=1}^{N}\left[\frac{\left(1-|\boldsymbol{M}_n|^2\right)\left(F_{ni}\tilde{R}_{ni}\right)}{R_n^2\left(1-\boldsymbol{M}_n\cdot\tilde{\boldsymbol{R}}_n\right)^3}\right]\Bigg\}_e, \end{aligned} \tag{21}$$

where the subscript n denotes the nth equivalent source. Here, q_n is the source strength and $\dot{q}_n$ its time derivative evaluated at the source time. The vector $\boldsymbol{y}_n$ specifies the source location, and $R_n = |\boldsymbol{x}-\boldsymbol{y}_n|$ is the distance from the source to the observer. The unit vector $\tilde{\boldsymbol{R}}_n = (\boldsymbol{x}-\boldsymbol{y}_n)/R_n$ defines the source-to-observer direction. The Mach vector $\boldsymbol{M}_n$ and its time derivative $\dot{\boldsymbol{M}}_n$ are likewise evaluated at the retarded time τ_e. The subscript "e" indicates that all quantities within the brackets are to be evaluated at this retarded time.

In practical applications, acoustic pressure measurements are available only at discrete time instances. Accordingly, the observation time is discretized as

$$t^k = t^1 + (k-1)\Delta t, \quad k = 1,2,\ldots,K, \tag{22}$$

where Δt denotes the temporal sampling interval and K is the total number of sampling points. Following the same approach, the source time is discretized such that

$$\tau^l = \tau^1 + (l-1)\Delta\tau, \quad l = 1,2,\ldots,L. \tag{23}$$

To correlate the source emission times with the observation times, the following retarded-time relation is employed

$$\tau_n^k = t^k - \frac{R_n}{c}. \tag{24}$$

As τ_n^k generally does not coincide with the discretized source times τ^l, interpolation is required to evaluate the source strength and its time derivative at arbitrary emission times. A first-order Lagrange interpolation is adopted, such that:

$$\begin{aligned} q_n(\tau_n^k) &= \sum_{l=1}^{L}\zeta_l(\tau_n^k)\,q_n^l, \qquad \dot{q}_n(\tau_n^k) = \sum_{l=1}^{L}\frac{\partial\zeta_l}{\partial\tau}(\tau_n^k)\,q_n^l, \\ F_{ni}(\tau_n^k) &= \sum_{l=1}^{L}\zeta_l(\tau_n^k)\,F_{ni}^l, \qquad \dot{F}_{ni}(\tau_n^k) = \sum_{l=1}^{L}\frac{\partial\zeta_l}{\partial\tau}(\tau_n^k)\,F_{ni}^l, \end{aligned} \tag{25}$$

where q_n^l is the strength of the nth source at time τ^l, F_{ni}^l denotes the ith component of the corresponding dipole source strength at the same time, and $\zeta^l(\tau)$ is the interpolation kernel defined by:

$$\zeta^l(\tau)=\begin{cases}(\tau-\tau^{l-1})/\Delta t, & \tau^{l-1}\le\tau\le\tau^l,\\ (\tau^{l+1}-\tau)/\Delta t, & \tau^l\le\tau\le\tau^{l+1},\\ 0, & \text{otherwise},\end{cases} \tag{26}$$

and its derivative is given by:

$$\frac{\partial\zeta^l(\tau)}{\partial\tau}=\begin{cases}1/\Delta t, & \tau^{l-1}\le\tau\le\tau^l,\\ -1/\Delta t, & \tau^l\le\tau\le\tau^{l+1},\\ 0, & \text{otherwise}.\end{cases} \tag{27}$$

Substituting the interpolated source strengths into the discrete acoustic pressure formulation Eq. (21) yields a linear system, given by

$$\begin{aligned}p'\left(\boldsymbol{x},t^k\right)=&\frac{1}{4\pi}\sum_{n=1}^{N}\sum_{l=1}^{k}\left\{\frac{1}{R_n\left(1-\boldsymbol{M}_n\cdot\tilde{\boldsymbol{R}}_n\right)^2}\frac{\partial\zeta^l\left(\tau_n^k\right)}{\partial\tau}q_n^l\right.\\&+\frac{\dot{\boldsymbol{M}}_n\cdot\tilde{\boldsymbol{R}}_n}{R_n\left(1-\boldsymbol{M}_n\cdot\tilde{\boldsymbol{R}}_n\right)^3}\zeta^l\left(\tau_n^k\right)q_n^l+\frac{c_0\left(\boldsymbol{M}_n\cdot\tilde{\boldsymbol{R}}_n-|\boldsymbol{M}_n|^2\right)}{R_n^2\left(1-\boldsymbol{M}_n\cdot\tilde{\boldsymbol{R}}_n\right)^3}\zeta^l\left(\tau_n^k\right)q_n^l\\&+\frac{1}{c_0}\frac{\tilde{R}_{ni}}{R_n\left(1-\boldsymbol{M}_n\cdot\tilde{\boldsymbol{R}}_n\right)^2}\frac{\partial\zeta^l\left(\tau_n^k\right)}{\partial\tau}F_{ni}^l-\frac{M_{ni}}{R_n^2\left(1-\boldsymbol{M}_n\cdot\tilde{\boldsymbol{R}}_n\right)^2}\zeta^l\left(\tau_n^k\right)F_{ni}^l\\&\left.+\frac{1}{c_0}\frac{(\dot{\boldsymbol{M}}_n\cdot\tilde{\boldsymbol{R}}_n)\tilde{R}_{ni}}{R_n\left(1-\boldsymbol{M}_n\cdot\tilde{\boldsymbol{R}}_n\right)^3}\zeta^l\left(\tau_n^k\right)F_{ni}^l+\frac{(1-|\boldsymbol{M}_n|^2)\tilde{R}_{ni}}{R_n^2\left(1-\boldsymbol{M}_n\cdot\tilde{\boldsymbol{R}}_n\right)^3}\zeta^l\left(\tau_n^k\right)F_{ni}^l\right\},\end{aligned} \tag{28}$$

where all source-dependent quantities are evaluated at the corresponding retarded times τ_n^k.

For notational compactness, the kernel function is defined as:

$$\begin{aligned}g_n^l\left(\tau_n^k\right)=&\frac{1}{R_n\left(1-\boldsymbol{M}_n\cdot\tilde{\boldsymbol{R}}_n\right)^2}\frac{\partial\zeta^l\left(\tau_n^k\right)}{\partial\tau}+\frac{\dot{\boldsymbol{M}}_n\cdot\tilde{\boldsymbol{R}}_n}{R_n\left(1-\boldsymbol{M}_n\cdot\tilde{\boldsymbol{R}}_n\right)^3}\zeta^l\left(\tau_n^k\right)\\&+\frac{c_0\left(\boldsymbol{M}_n\cdot\tilde{\boldsymbol{R}}_n-|\boldsymbol{M}_n|^2\right)}{R_n^2\left(1-\boldsymbol{M}_n\cdot\tilde{\boldsymbol{R}}_n\right)^3}\zeta^l\left(\tau_n^k\right),\end{aligned} \tag{29}$$

and the kernel function associated with the dipole term is given by the expression

$$\begin{aligned}h_{ni}^l\left(\tau_n^k\right)=&\frac{1}{c_0}\frac{\tilde{R}_{ni}}{R_n\left(1-\boldsymbol{M}_n\cdot\tilde{\boldsymbol{R}}_n\right)^2}\frac{\partial\zeta^l\left(\tau_n^k\right)}{\partial\tau}-\frac{M_{ni}}{R_n^2\left(1-\boldsymbol{M}_n\cdot\tilde{\boldsymbol{R}}_n\right)^2}\zeta^l\left(\tau_n^k\right)\\&+\frac{1}{c_0}\frac{\left(\dot{\boldsymbol{M}}_n\cdot\tilde{\boldsymbol{R}}_n\right)\tilde{R}_{ni}}{R_n\left(1-\boldsymbol{M}_n\cdot\tilde{\boldsymbol{R}}_n\right)^3}\zeta^l\left(\tau_n^k\right)+\frac{\left(1-|\boldsymbol{M}_n|^2\right)\tilde{R}_{ni}}{R_n^2\left(1-\boldsymbol{M}_n\cdot\tilde{\boldsymbol{R}}_n\right)^3}\zeta^l\left(\tau_n^k\right).\end{aligned} \tag{30}$$

The discrete acoustic pressure can be expressed compactly as:

$$p'\left(\boldsymbol{x},t^k\right)=\sum_{n=1}^{N}\sum_{l=1}^{k}\left[g_n^l\left(\tau_n^k\right)q_n^l+h_{ni}^l\left(\tau_n^k\right)F_{ni}^l\right]. \tag{31}$$

Further, Eq. (31) is written in the following matrix form:

$$\begin{aligned}p'(\boldsymbol{x},t^k)=&g^{1k}q^1+g^{2k}q^2+\cdots+g^{lk}q^l+\cdots+g^{kk}q^k\\&+h^{1k}F^1+h^{2k}F^2+\cdots+h^{lk}F^l+\cdots+h^{kk}F^k,\end{aligned} \tag{32}$$

where

$$\begin{aligned}\boldsymbol{g}^{lk}=&\left[\ g_1^l\left(\tau_1^k\right)\quad\cdots\quad g_n^l\left(\tau_n^k\right)\quad\cdots\quad g_N^l\left(\tau_N^k\right)\ \right],\\ \boldsymbol{h}^{lk}=&\left[\ h_{11}^l\left(\tau_1^k\right)\ \cdots\ h_{N1}^l\left(\tau_N^k\right)\ h_{12}^l\left(\tau_1^k\right)\ \cdots\right.\\&\left.h_{N2}^l\left(\tau_N^k\right)\ h_{13}^l\left(\tau_1^k\right)\ \cdots\ h_{N3}^l\left(\tau_N^k\right)\ \right].\end{aligned} \tag{33}$$

$$\begin{aligned}\boldsymbol{q}^l=&\left[\ q_1^l\left(\tau_1^k\right)\quad\cdots\quad q_n^l\left(\tau_n^k\right)\quad\cdots\quad q_N^l\left(\tau_N^k\right)\ \right]^{\mathrm{T}},\\ \boldsymbol{F}^l=&\left[\ F_{11}^l\left(\tau_1^k\right)\ \cdots\ F_{N1}^l\left(\tau_N^k\right)\ F_{12}^l\left(\tau_1^k\right)\ \cdots\right.\\&\left.F_{N2}^l\left(\tau_N^k\right)\ F_{13}^l\left(\tau_1^k\right)\ \cdots\ F_{N3}^l\left(\tau_N^k\right)\ \right]^{\mathrm{T}}.\end{aligned} \tag{34}$$

The superscript T denotes the transpose of a matrix. Assuming that the measurement array contains $\bar{Q}$ measurement points, Eq. (32) is applied to each measurement point and the following extended matrix equation is obtained:

$$\begin{aligned}\boldsymbol{P}^k=&\boldsymbol{G}^{1k}\boldsymbol{q}^1+\boldsymbol{G}^{2k}\boldsymbol{q}^2+\cdots+\boldsymbol{G}^{lk}\boldsymbol{q}^l+\cdots+\boldsymbol{G}^{kk}\boldsymbol{q}^k\\&+\boldsymbol{H}^{1k}\boldsymbol{F}^1+\boldsymbol{H}^{2k}\boldsymbol{F}^2+\cdots+\boldsymbol{H}^{lk}\boldsymbol{F}^l+\cdots+\boldsymbol{H}^{kk}\boldsymbol{F}^k,\end{aligned} \tag{35}$$

where

$$\boldsymbol{P}^k = \left[\ p'\left(\boldsymbol{x}_1, t^k\right) \quad p'\left(\boldsymbol{x}_2, t^k\right) \quad \cdots \quad p'\left(\boldsymbol{x}_{\bar{q}}, t^k\right) \quad \cdots \quad p'\left(\boldsymbol{x}_{\bar{Q}}, t^k\right)\ \right]^{\mathrm{T}}, \tag{36}$$

$$\boldsymbol{G}^{lk} = \left[\ \left(\boldsymbol{g}_1^{lk}\right)^{\mathrm{T}} \quad \left(\boldsymbol{g}_2^{lk}\right)^{\mathrm{T}} \quad \cdots \quad \left(\boldsymbol{g}_{\bar{q}}^{lk}\right)^{\mathrm{T}} \quad \cdots \quad \left(\boldsymbol{g}_{\bar{Q}}^{lk}\right)^{\mathrm{T}}\ \right]^{\mathrm{T}}. \tag{37}$$

$$\boldsymbol{H}^{lk} = \left[\ \left(\boldsymbol{h}_1^{lk}\right)^{\mathrm{T}} \quad \left(\boldsymbol{h}_2^{lk}\right)^{\mathrm{T}} \quad \cdots \quad \left(\boldsymbol{h}_{\bar{q}}^{lk}\right)^{\mathrm{T}} \quad \cdots \quad \left(\boldsymbol{h}_{\bar{Q}}^{lk}\right)^{\mathrm{T}}\ \right]^{\mathrm{T}}. \tag{38}$$

Eq. (35) is further applied to all time steps and the following matrix equation is obtained:

$$\overleftrightarrow{\boldsymbol{P}} = \overleftrightarrow{\boldsymbol{A}}\,\overleftrightarrow{\boldsymbol{X}}, \tag{39}$$

where the augmented system matrix and unknown vector are defined as

$$\overleftrightarrow{\boldsymbol{A}} = \left[\overleftrightarrow{\boldsymbol{G}} \quad \overleftrightarrow{\boldsymbol{H}}\right], \qquad \overleftrightarrow{\boldsymbol{X}} = \begin{bmatrix}\overleftrightarrow{\boldsymbol{Q}} \\ \overleftrightarrow{\boldsymbol{F}}\end{bmatrix}. \tag{40}$$

Eq. (39) represents a linear system that relates the equivalent source strengths at all source time steps ($N \times K$ source strengths) and the measured sound pressures at all observation time steps ($\bar{Q} \times K$ measured sound pressures). Then, the equivalent source strengths on the rotating sources plane for all source time steps can be computed from the sampled values of the acoustic pressure at the measurement points by inverting Eq. (39) as:

$$\overleftrightarrow{\boldsymbol{X}} = \left(\overleftrightarrow{\boldsymbol{A}}\right)^{+} \boldsymbol{P}. \tag{41}$$

However, the inverse of matrix $\overleftrightarrow{\boldsymbol{A}}$ is often ill-conditioned due to the measurement geometry and the properties of the operator itself, e.g., strong column correlation and rapidly decaying singular values [45,46]. To stabilize the solution, spatiotemporal regularization with a mixed norm is introduced into the source identification framework:

$$\tilde{\boldsymbol{X}} = \underset{\overleftrightarrow{\boldsymbol{X}}}{\operatorname{argmin}} \left\| \overleftrightarrow{\boldsymbol{P}} - \overleftrightarrow{\boldsymbol{A}}\,\overleftrightarrow{\boldsymbol{X}} \right\|_2^2 + \lambda \|\boldsymbol{X}\|_{\alpha,\beta}^{\beta}, \tag{42}$$

where $\|\boldsymbol{X}\|_{\alpha,\beta}^{\beta}$ is the spatiotemporal regularization term with a mixed norm. The coefficients α and β are the norm parameters corresponding to space and time, respectively. Their selection depends on the prior knowledge of the spatial and temporal characteristics of the target acoustic signal. The regularization parameter λ is selected automatically using the L-curve criterion [47]. The spatiotemporal regularization term with a mixed norm is defined as:

$$\|\boldsymbol{X}\|_{\alpha,\beta}^{\beta} = \sum_{k=1}^{K} \left(\sum_{n=1}^{N} |\boldsymbol{X}_n^k|^{\alpha} \right)^{\frac{\beta}{\alpha}}, \tag{43}$$

where k denotes the kth sound source, and n denotes the nth time step. Since the minimization problem involving the regularization term admits an explicit solution, Eq. (42) can be solved using the generalized iterative reweighted least squares algorithm [48,49]. This approach transforms the mixed-norm formulation into an l_2 norm form by converting $\|\boldsymbol{X}\|_{\alpha,\beta}^{\beta}$ into $\|\hat{\boldsymbol{W}}\overleftrightarrow{\boldsymbol{X}}\|_2^2$, resulting in:

$$\tilde{\boldsymbol{X}} = \underset{\tilde{\boldsymbol{X}}}{\operatorname{argmin}} \left\| \overleftrightarrow{\boldsymbol{P}} - \overleftrightarrow{\boldsymbol{A}}\,\overleftrightarrow{\boldsymbol{X}} \right\|_2^2 + \lambda \left\| \hat{\boldsymbol{W}}\overleftrightarrow{\boldsymbol{X}} \right\|_2^2, \tag{44}$$

where $\hat{\boldsymbol{W}}$ is a diagonal matrix:

$$\hat{\boldsymbol{W}} = \operatorname{diag}\left(\left(\sqrt{W_{ni}^k W^k} \right)_{\substack{k=1,\ldots,K \\ i=0,1,2,3 \\ n=1,\ldots,N}} \right), \tag{45}$$

where $i = 0$ corresponds to the monopole coefficient q_n^k, and $i = 1, 2, 3$ correspond to the three components of the dipole coefficient F_{ni}^k and

$$W_{ni}^k = \begin{cases} \left|X_{ni}^k\right|^{\alpha-2}, & \left|X_{ni}^k\right| \geq \varepsilon, \\ \varepsilon^{\alpha-2}, & \text{otherwise}, \end{cases} \tag{46}$$

$$W^k = \begin{cases} \left[\left\| \left(\boldsymbol{X}^k\right)^{\mathrm{T}} \right\|_{\alpha}^{\alpha} \right]^{\beta/\alpha-1}, & \left\| \left(\boldsymbol{X}^k\right)^{\mathrm{T}} \right\|_{\alpha}^{\alpha} \geq \varepsilon^2 \\ (\varepsilon^2)^{\beta/\alpha-1}, & \text{otherwise}. \end{cases} \tag{47}$$

To prevent the weight values W_{ni}^k and W^k from approaching infinity, a small positive constant ε is added in Eqs. (46) and (47).

The explicit solution of Eq. (44) can be written in the following form:

$$\widetilde{\boldsymbol{X}} = \left(\overleftrightarrow{\boldsymbol{A}}^{\mathrm{H}} \overleftrightarrow{\boldsymbol{A}} + \lambda \overleftrightarrow{\boldsymbol{W}} \right)^{-1} \overleftrightarrow{\boldsymbol{A}}^{\mathrm{H}} \overleftrightarrow{\boldsymbol{P}}, \tag{48}$$

where the symbol "H" means the Hermitian transpose, $\overleftrightarrow{\boldsymbol{W}} = \hat{\boldsymbol{W}}^{\mathrm{H}} \hat{\boldsymbol{W}}$. Since the computation of the weight matrix $\overleftrightarrow{\boldsymbol{W}}$ requires knowledge of the value of X_{ni}^{k}, which means that the optimal solution to the minimization problem in Eq. (48) must be obtained through an iterative process:

$$\widetilde{\boldsymbol{X}}^{(s)} = \left(\overleftrightarrow{\boldsymbol{A}}^{\mathrm{H}} \overleftrightarrow{\boldsymbol{A}} + \lambda \overleftrightarrow{\boldsymbol{W}}^{(s-1)} \right)^{-1} \overleftrightarrow{\boldsymbol{A}}^{\mathrm{H}} \overleftrightarrow{\boldsymbol{P}}, \tag{49}$$

where s denotes the iteration number; $\widetilde{\boldsymbol{X}}^{(s)}$ represents the solution at the s-th iteration; $\overleftrightarrow{\boldsymbol{W}}^{(s-1)}$ denotes the weight matrix at the (s-1)-th iteration, which is composed of the reconstructed source strength $\widetilde{\boldsymbol{X}}^{(s-1)}$ from the (s-1)-th iteration.

The initial solution $\widetilde{\boldsymbol{X}}^{(0)}$ of the iterative process can be estimated using standard Tikhonov regularization [50], which has an explicit solution and corresponds to $\alpha = 2$, $\beta = 2$, i.e.:

$$\tilde{\boldsymbol{X}}^{(0)} = \underset{\tilde{\boldsymbol{X}}}{\operatorname{argmin}} \left\| \overleftrightarrow{\boldsymbol{P}} - \overleftrightarrow{\boldsymbol{A}} \overleftrightarrow{\boldsymbol{X}} \right\|_2^2 + \lambda \left\| \hat{\boldsymbol{W}} \overleftrightarrow{\boldsymbol{X}} \right\|_2^2. \tag{50}$$

The functional at the s-th iteration is:

$$J\left(\tilde{\boldsymbol{X}}^{(s)}\right) = \left\| \overleftrightarrow{\boldsymbol{P}} - \overleftrightarrow{\boldsymbol{A}} \tilde{\boldsymbol{X}}^{(s)} \right\|_2^2 + \lambda \left\| \overleftrightarrow{\boldsymbol{W}}^{(s-1)} \tilde{\boldsymbol{X}}^{(s)} \right\|_2^2. \tag{51}$$

Accordingly, the relative variation δ of the functional J between two successive generations can be expressed as:

$$\delta = \left| 1 - \frac{J\left(\widetilde{\boldsymbol{X}}^{(s)}\right)}{J\left(\widetilde{\boldsymbol{X}}^{(s-1)}\right)} \right|, \tag{52}$$

when the relative change δ is less than or equal to the given tolerance, or the algorithm reaches the maximum number of iterations, the iterative process terminates.

The mixed-norm spatiotemporal regularization technique is highly flexible, allowing various source distributions and different excitation signals to be handled within a unified framework. In practical applications, since the distribution of rotating noise sources is unknown, finding suitable values for α and β is not straightforward. Empirically, if the sources are spatially concentrated, choosing $\alpha \leq 1$ promotes sparsity in the solution [49,51]; if the source strength signals are continuous over the considered time duration, setting $\beta = 2$ is reasonable.

3. Numerical assessment

3.1. Simulation setup

To evaluate the accuracy and robustness of the proposed time-domain inverse method, numerical simulations are performed with rotating monopole and dipole sources serving as benchmark cases. The analysis addresses three principal objectives: the real-time localization of the rotating source, the reconstruction of its time-varying strength, and the prediction of the resulting acoustic field. The method is tested under varying rotational speeds (1000 rpm, 3000 rpm, and 5000 rpm) and signal-to-noise ratio (SNR) conditions ranging from 0 to 30 dB. The details of the simulation setup, including spatial discretization and the configuration of the computational domain, are illustrated in Fig. 2.

The simulation configuration employs a planar measurement array composed of 90 sensors located on the plane $x_3 = 0.02$ m. The array is arranged in three concentric circular rings of radii 0.1 m, 0.2 m, and 0.3 m, each containing thirty uniformly spaced sensors, thereby ensuring adequate spatial sampling of the acoustic field. To model the radiating source distribution, 30 equivalent sources are placed on the $x_3 = 0$ m plane within the source region. These sources are uniformly distributed across three circular rings of the same radii as the measurement array (ten sources per ring), and rotate synchronously with the actual sound sources to emulate their radiation characteristics.

Four rotating sources, denoted S1, S2, F_a and F_b, are positioned at $(0.2, 0, 0)$, $(-0.2, 0, 0)$ m, $(0.2, 0, 0)$ and $(-0.2, 0, 0)$ m, and coincide with four of the equivalent source locations. To assess the predictive capability of the inverse method, four monitoring points, labelled M1 to M4, are placed at

$$(0.3, 0, 0.01)\ \mathrm{m}, (0, 0.3, 0.01)\ \mathrm{m}, (-0.3, 0, 0.01)\ \mathrm{m}, (0, -0.3, 0.01)\ \mathrm{m}.$$

These points are located between the source plane and the measurement plane, and serve as validation probes for reconstructed pressure fields.

Reconstruction proceeds by using the acoustic pressure signals recorded at the measurement array to infer the time-dependent strengths of all equivalent sources via the proposed inverse method. These estimated source strengths are then used as inputs to a

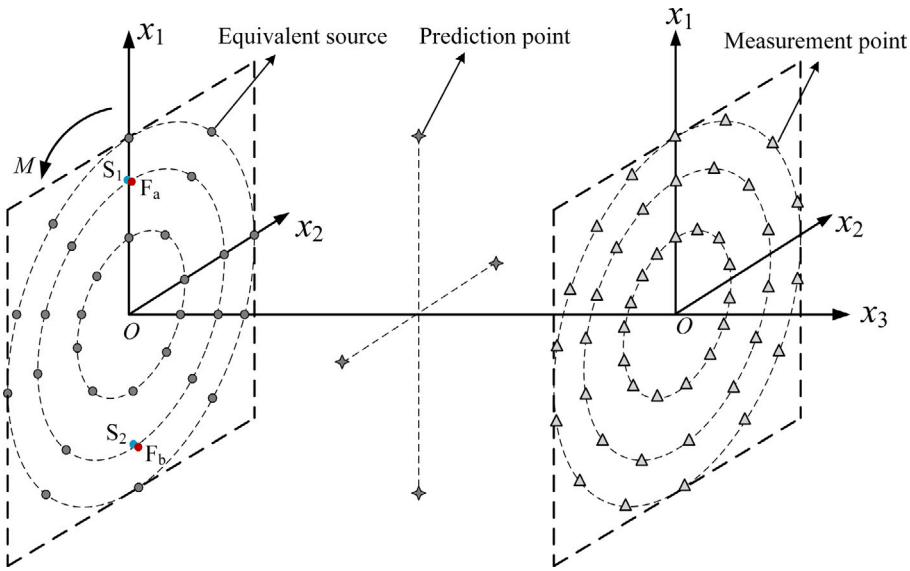

Fig. 2. Geometric configuration used in the numerical simulations. The rotating monopole sources are represented by equivalent source points (solid circles) distributed on concentric rings around the origin O, with S_1 and S_2 denoting representative source locations. Dipole sources F_a and F_b are also considered and are collocated with the corresponding monopole sources at S_1 and S_2, respectively. Measurement points (triangles) are arranged on three concentric rings to capture the acoustic field; each ring contains 30 measurement points, i.e, points in total, but for clarity only 15 points per ring, i.e, 45 points in total are shown. The remaining points are uniformly distributed on the same rings. Prediction points, denoted by stars, are placed outside the source region to evaluate reconstruction accuracy. The coordinate system (x_1, x_2, x_3) and the rotational Mach number M are also indicated.

forward acoustic model to compute the sound pressure at arbitrary field locations, including the prediction points. The reconstructed pressure field can thus be directly compared against simulated reference measurements to quantify accuracy. The overall simulation framework is designed to balance spatial sampling requirements, equivalent source modelling, and validation capabilities, thereby enabling a comprehensive evaluation of the inversion algorithm's performance.

3.2. Results at different rotational speeds

In order to analyse the performance of the proposed time-domain inverse method under different rotational speeds, three simulation cases are defined, where the rotational speeds of the sources are set to 1000 rpm, 3000 rpm, and 5000 rpm for Cases 1, 2, and 3, respectively. For the two rotating monopole sources, their source strength signals are defined as $S_1 = A\ \sin(2\pi f_s(1-(\tau_1-\mathrm{d}\tau)))$ and $S_2 = A\ \sin(2\pi f_s(1-(\tau_1-\mathrm{d}\tau)))$, and two dipole sources strength signals F_a and F_b are defined as

$$\begin{cases} F_{a1} = F_D\ \sin\left(2\pi f_s\theta\right), \\ F_{a2} = F_D\ \cos\left(2\pi f_s\theta + \phi\right), \\ F_{a3} = F_L\ \cos\left(2\pi f_s\theta\right)\ \exp\left(-[100\theta - 0.5]^2\right). \end{cases} \tag{53}$$

$$\begin{cases} F_{b1} = F_D\ \sin\left(2\pi f_s\theta + \phi\right), \\ F_{b2} = F_D\ \cos\left(2\pi f_s\theta\right), \\ F_{b3} = F_L\ \cos\left(2\pi f_s\theta\right)\ \exp\left(-[100\theta - 0.5]^2\right). \end{cases} \tag{54}$$

Where A, B denote the amplitude and f_s is the signal frequency. We define $\theta = (1-(\tau_1-\mathrm{d}\tau))$. The time delay $\tau_1 = t_1 - r_{\min}/c$, where $r_{\min}$ represents the minimum distance between the equivalent source surface and the measurement surface, and c is the speed of sound. The specific parameter values are given as $A = 0.001$ Pa, $F_D = 0.02$ N, $F_L = 0.01$ N, $f_s = 1000$ Hz, $\phi = \pi$, $c_0 = 343$ m/s. All cases are sampled at 12.8 kHz. To emulate realistic measurement noise, Gaussian white noise with a SNR of 30 dB is added to the simulated pressure data.

Based on the above simulation setup and the prescribed time-varying source strength signals, the radiated sound pressure from the rotating sources (used as input) can be calculated using Eq. (39). Furthermore, the prescribed time-varying source strength serves as a reference to evaluate the accuracy of the proposed method in reconstructing the source strength signals. Using these

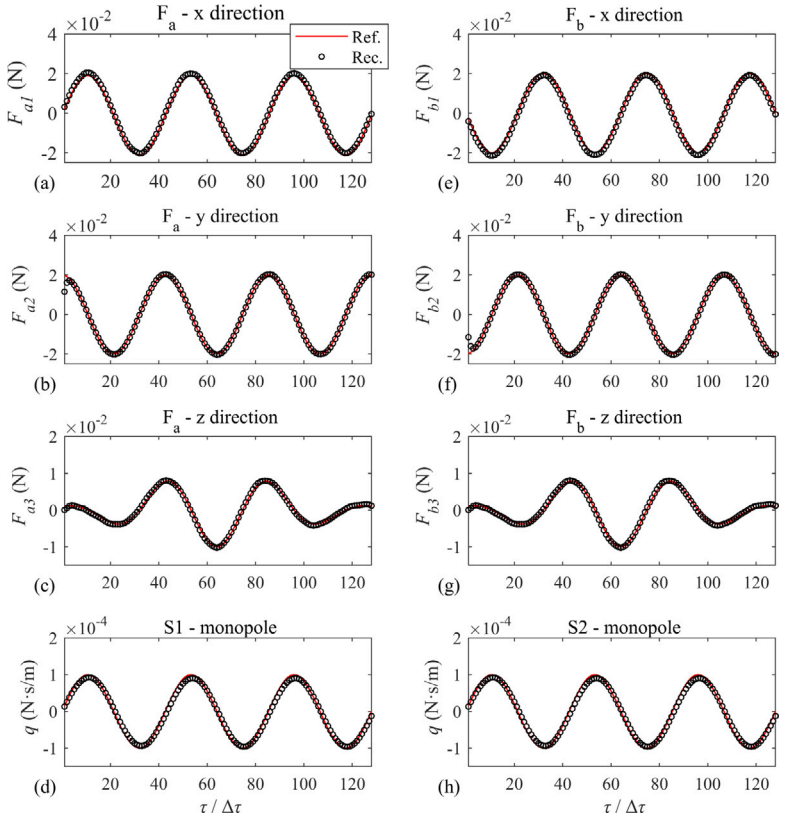

Fig. 3. Reconstructed and reference source strengths in Case 1 (1000 rpm). (a)–(c) Dipole source components F_{a1}, F_{a2}, and F_{a3};(d) monopole source strength S_1. (e)–(g) Dipole source components F_{b1}, F_{b2}, and F_{b3} at source S_2; (h) monopole source strength S_2. The figure illustrates the accuracy of the proposed time domain inverse method at the lowest tested rotational speed.

given signals, the theoretical sound pressure on the prediction surface can also be computed via Eq. (39), providing a benchmark for assessing the method's sound field prediction capability. To simulate real-world conditions, Gaussian white noise with a SNR of 30 dB is added to the radiated sound pressure signals. Here, SNR is defined as the ratio of the target sound signal power to the noise power, i.e.,

$$\mathrm{SNR} = 10\log_{10}\frac{P_s}{P_n}, \tag{55}$$

where P_s is the target signal power; P_n is the noise power.

Accuracy of source strength reconstruction. Figs. 3–5 present the time histories of the reconstructed source strength signals, obtained using Eq. (49) at three different rotational speeds and compared with their theoretical counterparts. It is seen that the reconstructed source strength signals for the two unsteady rotating sources agree well with the reference ones during the entire time period for all three speed cases, confirming the effectiveness of the proposed time-domain inverse method based on the Farassat integral form of the FW–H equation. This agreement demonstrates the method's capability to capture the dynamics of rotating sources with time-varying strengths across different rotational speeds.

Source localization capability. The proposed method also enables accurate spatial localization of rotating sources. First, Eq. (41) is applied to the measured data at each time step to reconstruct the equivalent source strengths. Then, the reconstructed source strengths are mapped onto the actual source space to obtain the source strength distribution at each time instant. To clearly display the localization results of the rotating sources, Figs. 6–8 present the spatial distribution of all equivalent source strengths at four different time steps under different rotational speed conditions. The white squares in the figures represent the actual positions of the two rotating sources, while the red regions highlight areas with high equivalent source strength. From the spatial distribution results, it is evident that the equivalent source strengths reconstructed by the proposed method are highly concentrated in space and exhibit peaks at the actual source locations. This indicates that the method not only reconstructs the source strength accurately but also achieves precise spatial localization, greatly enhancing the ability to identify and monitor noise sources.

Sound field prediction performance. Beyond localization, the reconstructed source strengths can be used to predict the sound field. Specifically, the equivalent source strengths are first obtained at each time step using the ESM. These reconstructed source strength

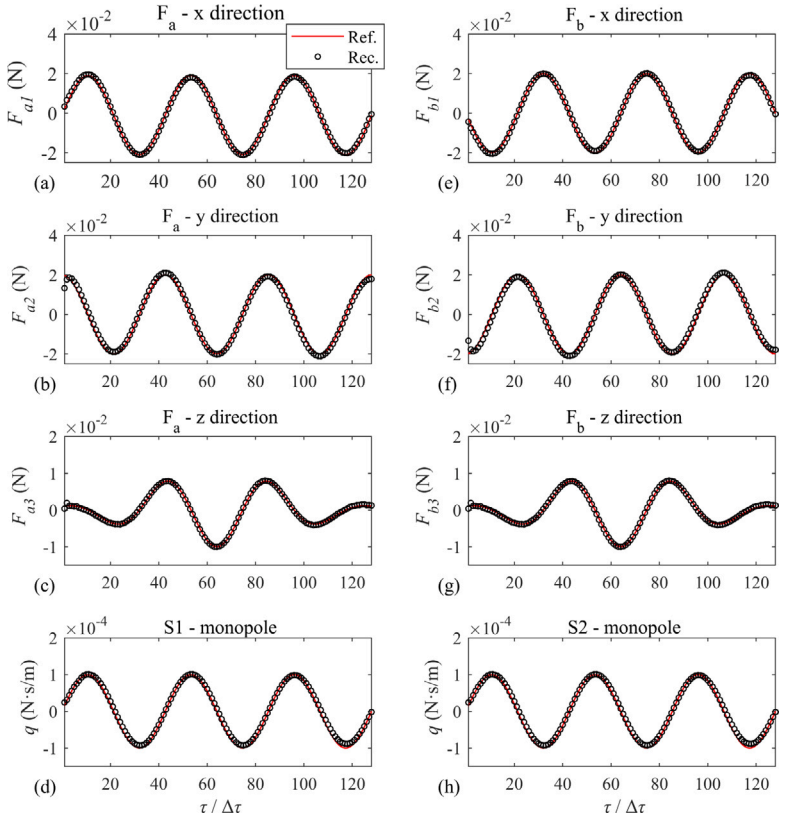

Fig. 4. Reconstructed and reference source strengths in Case 2 (3000 rpm). (a)–(c) Dipole source components F_{a1}, F_{a2}, and F_{a3}; (d) monopole source strength S_1. (e)–(g) Dipole source components F_{b1}, F_{b2}, and F_{b3} at source S_2; (h) monopole source strength S_2. The figure illustrates the accuracy of the proposed time domain inverse method at the intermediate rotational speed.

signals, along with the spatial relationships (including distance and angle) between the prediction points and the equivalent source points, are used to calculate the sound pressure at the prediction points using Eq. (39). This process allows for an accurate simulation of the source radiation effects and the prediction of the sound field changes at different locations.

Figs. 9–11 show the comparison results between the reconstructed source strength signals and theoretical sound fields at different prediction points. As shown, the predicted sound pressures closely match the theoretical values, confirming that the reconstructed source signals can accurately capture the temporal variations of the sound field. This demonstrates that the proposed reconstruction method remains effective even under dynamically changing source conditions, providing results consistent with theoretical predictions. The validation highlights not only the accuracy of the reconstructed source strengths but also the method's potential for high-precision sound field prediction, particularly in scenarios involving rotating sources.

3.3. Robustness under noisy conditions

To further evaluate the robustness of the proposed method under realistic measurement conditions, additional simulations are conducted by introducing Gaussian white noise with different SNRs. To quantify the reconstruction accuracy, the phase evaluation factor E_p and the amplitude evaluation factor E_a are adopted as accuracy/error indicators, defined as follows:

$$E_p = \frac{\left|\boldsymbol{Q}_{\mathrm{th}}^{\mathrm{T}}\boldsymbol{Q}_{\mathrm{re}}\right|}{\sqrt{\left(\boldsymbol{Q}_{\mathrm{th}}^{\mathrm{T}}\boldsymbol{Q}_{\mathrm{th}}\right)\left(\boldsymbol{Q}_{\mathrm{re}}^{\mathrm{T}}\boldsymbol{Q}_{\mathrm{re}}\right)}}, \tag{56}$$

$$E_a = \frac{\left|\sqrt{\boldsymbol{Q}_{\mathrm{th}}^{\mathrm{T}}\boldsymbol{Q}_{\mathrm{th}}} - \sqrt{\boldsymbol{Q}_{\mathrm{re}}^{\mathrm{T}}\boldsymbol{Q}_{\mathrm{re}}}\right|}{\sqrt{\boldsymbol{Q}_{\mathrm{re}}^{\mathrm{T}}\boldsymbol{Q}_{\mathrm{re}}}}. \tag{57}$$

Here the superscript "T" denotes the transpose of matrix; $\boldsymbol{Q}_{\mathrm{th}}$ and $\boldsymbol{Q}_{\mathrm{re}}$ are the theoretical and reconstructed source strength, respectively; E_p indicates the phase similarity that should tend to 1, and E_a indicates the amplitude difference that should tend to 0.

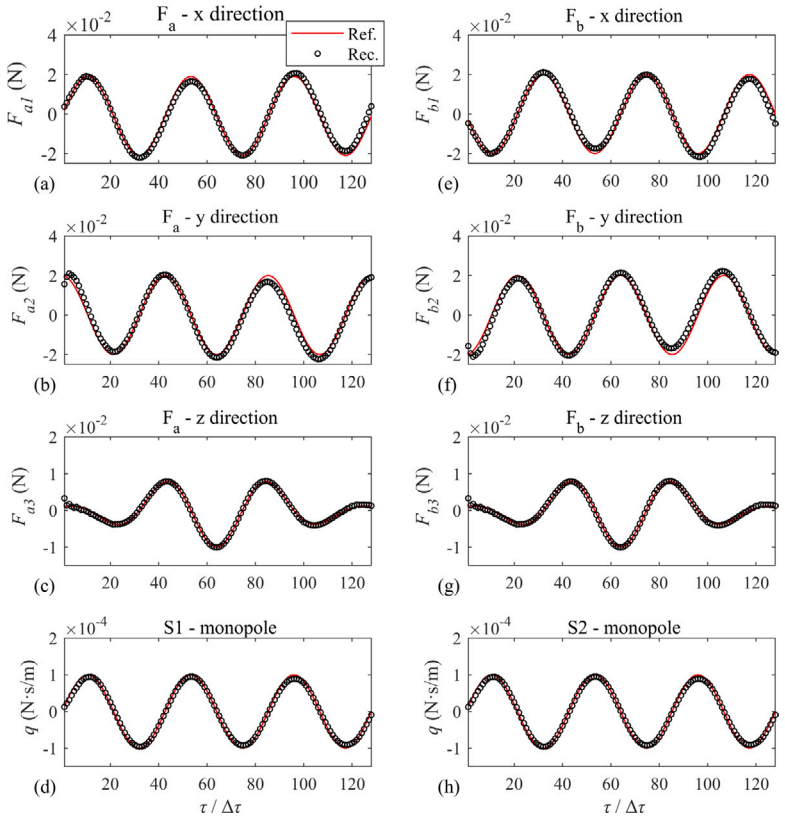

Fig. 5. Reconstructed and reference source strengths in Case 3 (5000 rpm). (a)–(c) Dipole source components F_{a1}, F_{a2}, and F_{a3}; (d) monopole source strength S_1. (e)–(g) Dipole source components F_{b1}, F_{b2}, and F_{b3} at source S_2; (h) monopole source strength S_2. The figure illustrates the accuracy of the proposed time domain inverse method at the highest tested rotational speed.

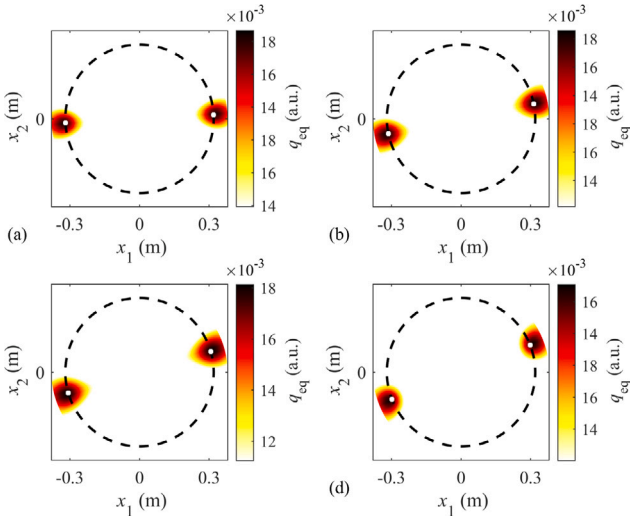

Fig. 6. Spatial localization results in Case 1 (1000 rpm). Distribution of reconstructed equivalent source strengths at four representative time steps: (a) τ_7, (b) τ_{25}, (c) τ_{35}, and (d) τ_{46}. The colour scale shows the reconstructed equivalent source strength q_{eq} in arbitrary units.

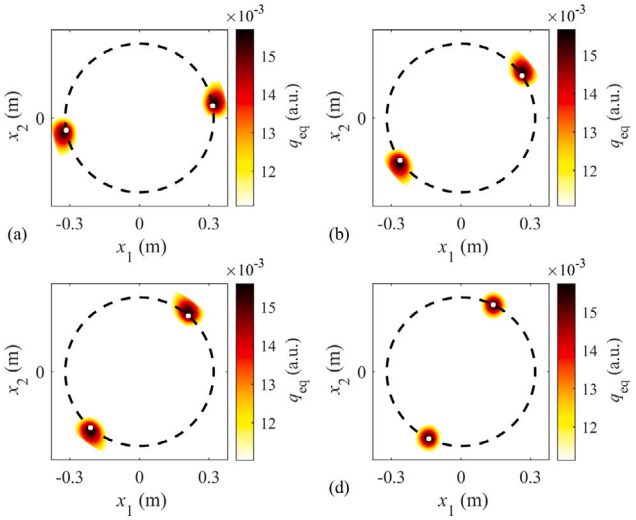

Fig. 7. Spatial localization results in Case 2 (3000 rpm). Distribution of reconstructed equivalent source strengths at four representative time steps: (a) τ_7, (b) τ_{25}, (c) τ_{35}, and (d) τ_{46}. The colour scale shows the reconstructed equivalent source strength q_{eq} in arbitrary units.

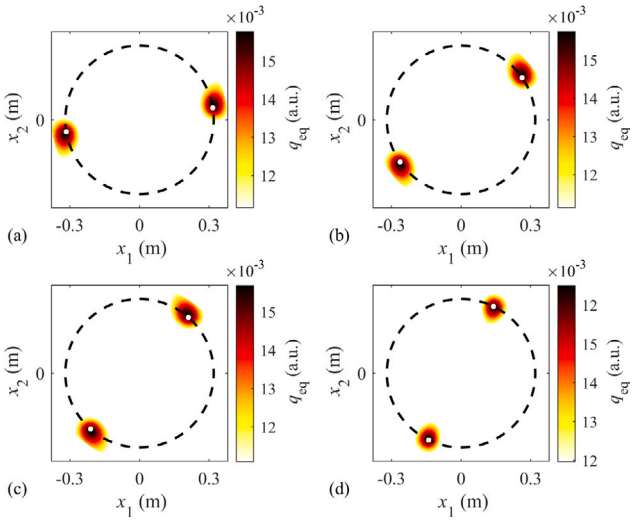

Fig. 8. Spatial localization results in Case 3 (5000 rpm). Distribution of reconstructed equivalent source strengths at four representative time steps: (a) τ_7, (b) τ_{25}, (c) τ_{35}, and (d) τ_{46}. The colour scale shows the reconstructed equivalent source strength q_{eq} in arbitrary units.

In practical usage of the inversion method, high background noise means lower reconstruction accuracy. Therefore, the convergence characteristics of the proposed time-domain method are examined by evaluating the accuracy indicators across different SNR levels. For comparison, a conventional Tikhonov-regularized inversion is implemented as a baseline. Fig. 12 shows the accuracy indicators of the presented methods in reconstructing the source signals at signal-to-noise ratios ranging from 0 dB to 30 dB. It can be observed that as the SNR decreases, the influences of noise on both the phase and amplitude indicators are slight. The phase indicators remain close to 1 and the amplitude indicators remain close to 0, indicating that the proposed method achieves accurate and robust reconstruction in noisy environments and consistently outperforms the Tikhonov baseline, especially at low SNR levels.

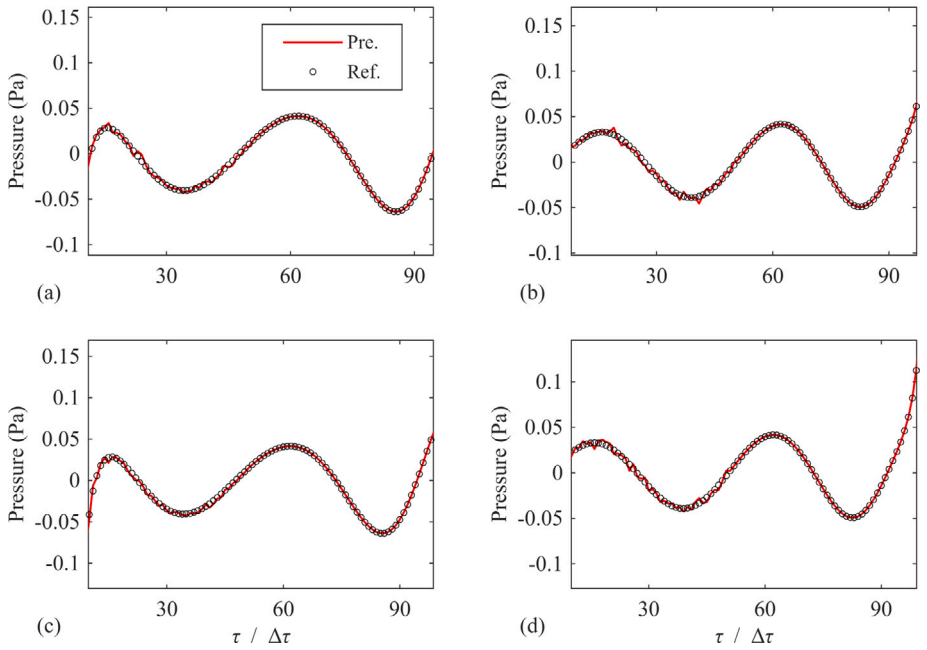

Fig. 9. Comparison of predicted and reference sound pressures at four prediction points in Case 1 (1000 rpm). (a) M1 at (0.3, 0, 0.01) m; (b) M2 at (0, 0.3, 0.01) m; (c) M3 at (−0.3, 0, 0.01) m; (d) M4 at (0, −0.3, 0.01) m.

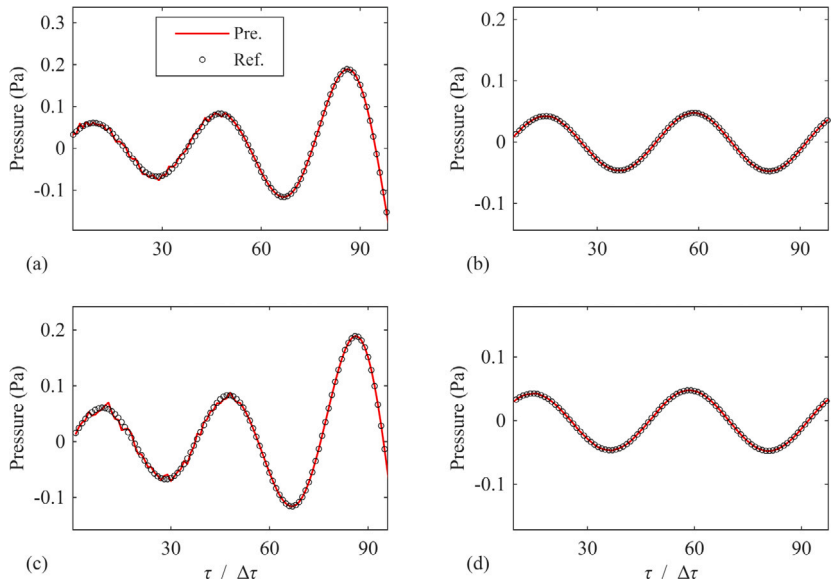

Fig. 10. Comparison of predicted and reference sound pressures at four prediction points in Case 2 (3000 rpm). (a) M1 at (0.3, 0, 0.01) m; (b) M2 at (0, 0.3, 0.01) m; (c) M3 at (−0.3, 0, 0.01) m; (d) M4 at (0, −0.3, 0.01) m.

4. Experimental evaluation

4.1. Experimental setup

Small UAV rotor experiments were carried out in a certified semi-anechoic chamber at Hefei University of Technology's Acoustics Research Facility to examine the localization accuracy and quantitative performance of the proposed time-domain method for unsteady rotating sound sources. The anechoic chamber provides an effective testing space of 8.5 m (L) × 7.6 m (W) × 5.5 m (H), with walls lined with FAIST's latest broadband composite acoustic absorbers. The chamber maintains a background noise level

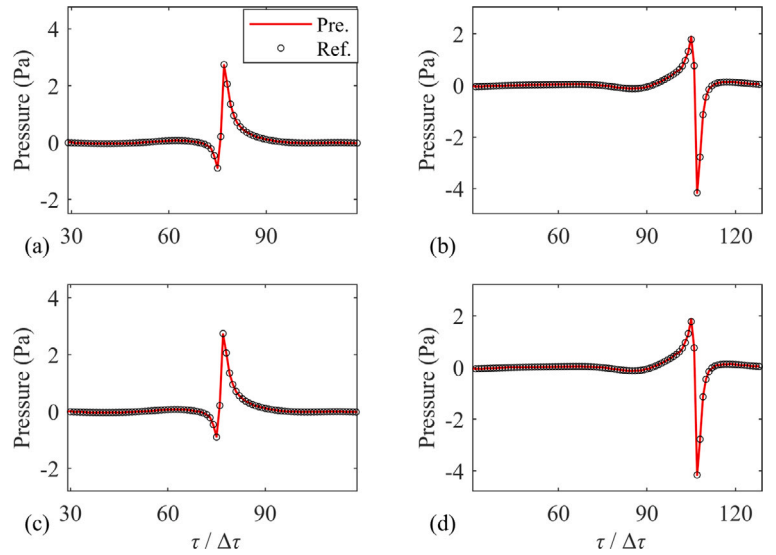

Fig. 11. Comparison of predicted and reference sound pressures at four prediction points in Case 3 (5000 rpm). (a) M1 at (0.3, 0, 0.01) m; (b) M2 at (0, 0.3, 0.01) m; (c) M3 at (−0.3, 0, 0.01) m; (d) M4 at (0, −0.3, 0.01) m.

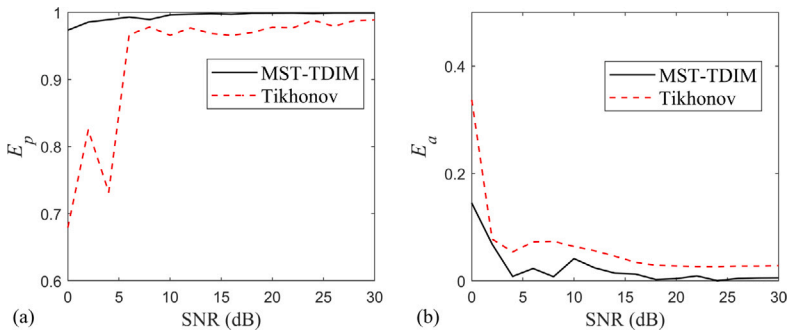

Fig. 12. Accuracy indicators across different SNR levels for the proposed time-domain method with mixed-norm regularization and conventional Tikhonov regularization.(a) Phase evaluation factor E_p, which approaches 1 for high phase similarity;(b) Amplitude evaluation factor E_a, which approaches 0 for low amplitude error.

below 18 dB(A) and achieves a low-frequency cutoff of 63 Hz. As shown in Fig. 13, this facility provides a controlled environment well-suited for sound source identification and control research.

The experimental setup is shown in Fig. 14. An UAV carbon-fibre rotor was employed. The rotor diameter was 0.4 m, the blade thickness was approximately 0.001 m, and the blade chord at 80% of the tip radius was 0.025 m. The rotor was driven by a low-noise direct-current brushless motor. A laser speedometer was used to measure the rotational speed, which was 999 rpm, corresponding to a tip Mach number of 0.0615.

During the acoustic-field measurements, as shown in Fig. 15, the rotor plane was carefully aligned to ensure that its rotation centre was at the same height as the centre of the microphone array. A global Cartesian coordinate system was established with the rotation centre of the rotor plane as the origin, where the positive x_3-axis points toward the measurement array and the positive x_1-axis is defined as the vertical upward direction. To characterize the radiated sound field, the rotor plane was discretized into 30 equivalent source points. These sources were uniformly distributed on three concentric rings with radii of 0.1 m, 0.2 m, and 0.3 m, respectively, with 10 source points on each ring, and were assumed to rotate synchronously with the rotor.

The acoustic measurements were performed using a double-ring microphone array comprising 60 omnidirectional microphones (BSWA MPA 451) in total (30 × 2), with an array diameter of 0.5 m. The two microphone rings were positioned at axial distances of 0.02 m and 0.04 m from the rotor disc. Consequently, a total of 60 sampling points were obtained, as shown in Fig. 15. To ensure consistent acoustic conditions between the two measurements, the pulse signal recorded by the laser tachometer was used as the trigger to synchronize the data acquisition system. A M"uller-BBM data acquisition unit equipped with 60-bit acquisition cards was employed to simultaneously record the sound pressure signals at the 60 microphone locations, with a sampling frequency of 10.24 kHz.

Fig. 13. Certified semi-anechoic chamber at the Acoustics Research Facility, Hefei University of Technology, where the rotating loudspeaker experiments were conducted. The chamber provides a controlled acoustic environment with broadband absorption and low background noise, suitable for sound source identification studies.

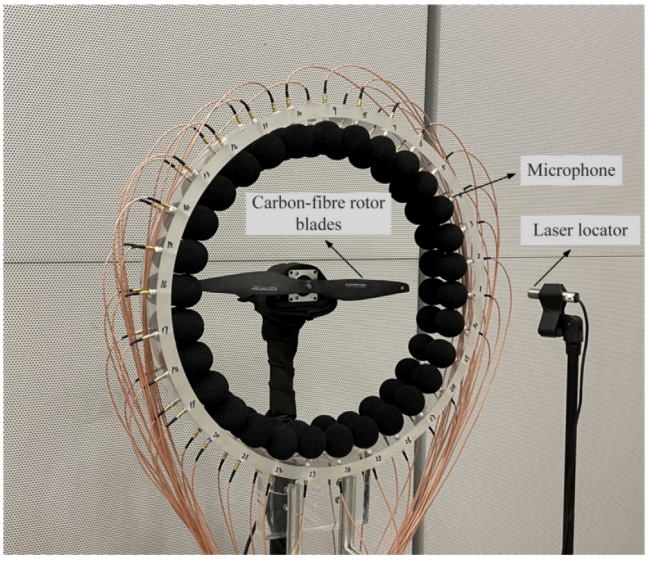

Fig. 14. Experimental setups for measuring the UAV rotating blade noise: the UAV blades and the microphone array, and the laser speedometer.

The analytical procedure processes the radiated sound pressure signals from the rotor blades acquired by the microphone array as input, establishes the transfer relationship between the measured sound pressure on the measurement plane and the equivalent source strengths on the source plane through Eq. (39), and inversely solves for the equivalent source strengths on the rotor blade surface, and subsequently predicts the complete radiation sound field

4.2. Experimental results and analysis

Accuracy of source strength reconstruction. Fig. 16 shows the time histories of the reconstructed source strength signals for the UAV rotor noise sources using MST-TDIM, including the x, y, and z components of the dipole noise source unsteady force signals in the Cartesian coordinate system, as well as the monopole noise source strength signals.

From Figs. 16(a), (e), (b), and (f), it can be observed that the force components in the x and y directions of the dipole source exhibit periodic harmonic characteristics, showing sinusoidal and cosine-like waveforms in the time domain. Additionally, the corresponding loading components on the two symmetrical blades display a complementary phase relationship. The formation of the orthogonal harmonic components described above arises from the process where the tangential loading, fixed to the rotating coordinate system, is periodically projected onto the stationary coordinate system as the blade rotates.

Figs. 16(c) and (g) show the z-direction force components of the dipole sources on the two blades. Combined with the coordinate system definition, the negative loading component represents the positive aerodynamic thrust generated by the rotor in operation.

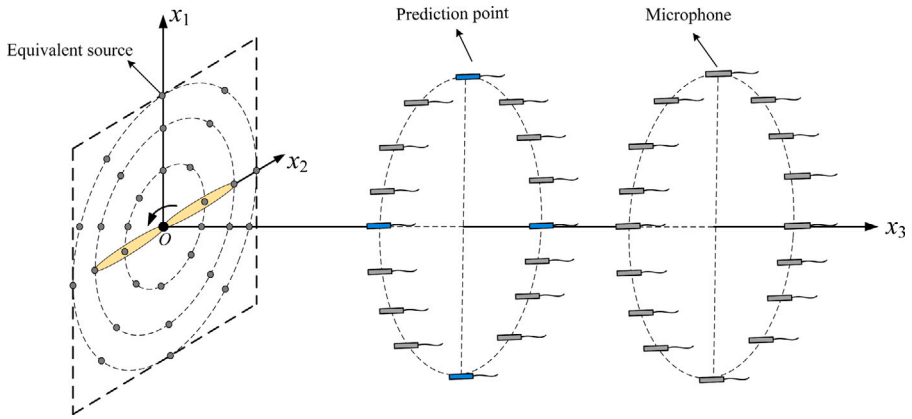

Fig. 15. Experimental setup for acoustic field measurements of the rotating blades. The rotor is mounted on the motor shaft and aligned with the global Cartesian coordinate system centred at the rotational axis O. The rotating source region is discretized into equivalent source points with solid circles distributed on concentric rings. A double-ring microphone array comprising 60 omnidirectional microphones (30 × 2) is employed to record the radiated sound field, with the two microphone rings located at axial distances of 0.02 m and 0.04 m from the source plane. Four additional reference microphones are positioned for validation at M1(0.2, 0, 0.02) m, M2(0, 0.2, 0.02) m, M3(−0.2, 0, 0.02) m, and M4(0, −0.2, 0.02) m. The coordinate system (x_1, x_2, x_3), equivalent sources, microphones, and reference sensors are all indicated schematically.

Additionally, the unsteady periodic fluctuations may be caused by aerodynamic interference between the rotating blades and the wake vortex system or by the uneven distribution of induced inflow in the plane of the rotor.

Figs. 16(d) and (h) show the reconstructed monopole source strengths on the two blades. The monopole source strength also exhibits unsteady periodic fluctuations, with its values consistently remaining in the negative range. This phenomenon characterizes the volume displacement effect produced by the rotor blade with a specific geometric thickness, continuously displacing the surrounding fluid during rotational motion. Furthermore, the periodic peak values appearing in the curves may be due to the unsteady variation of the local fluid mass flux during the blade's rotation.

A further analysis of Figs. 16(a)–(h) shows that, under the current operating condition with M = 0.0614, the dipole source strength dominates. In this case, to maintain thrust and torque balance at low rotational speeds, the rotor blades must endure relatively high levels of both steady and unsteady aerodynamic loading, which is the primary source of dipole sound radiation. In contrast, the monopole source provides a discernible yet supplementary contribution to the reconstruction results, consistent with the blade's thin geometry and the low volume acceleration of displaced fluid at low speeds. These results align with low-speed rotor sound radiation theory, confirming the experimental validity and MST-TDIM's ability to identify weak monopole contributions.

In previous work [36], neglecting the monopole mechanism under low Mach number conditions is a reasonable and effective approximation, providing a foundation for understanding the spatial distribution of aerodynamic loading noise. However, as the rotor's Mach number increases, the monopole contribution becomes more significant. Since monopole and dipole sources have distinct spatial radiation patterns, applying ST-TDIM at higher Mach numbers may produce false loading sources when fitting the thickness noise, creating artifacts in source localization and compromising quantitative accuracy. The MST-TDIM method, as an extension of ST-TDIM, overcomes this limitation by suppressing false-source interference and providing more accurate and physically meaningful reconstructions as monopole strength increases.

Source localization capability. Fig. 17 further illustrates the source localization results for the rotating blades at four different time steps, τ_{100}, τ_{200}, τ_{300}, and τ_{400}, showing that the MST-TDIM method is able to capture the source distribution on the blade surface at different time steps, with the reconstructed source energy being concentrated in the blade tip region. This spatial distribution arises from the higher rotational velocity at the blade tip and the greater rate of change of Mach number along the observer's direction, resulting in larger aerodynamic loads. Consequently, the blade tip region dominates sound radiation, confirming the accuracy of the MST-TDIM method in localizing the rotating blade's loading sources at different time steps.

Sound field prediction performance. To evaluate the acoustic field prediction capability of the MST-TDIM method, the sound pressure was predicted at four field points, namely M1 (0.2, 0, 0.02) m, M2 (0, 0.2, 0.02) m, M3 (−0.2, 0, 0.02) m, and M4 (0, −0.2, 0.02) m, using both ST-TDIM and MST-TDIM, and the results were compared with the measured signals, as shown in Fig. 18. The results show that both methods can effectively predict the overall periodic variation of the sound pressure at the field points, with MST-TDIM providing relatively more stable predictions. Specifically, when approaching the sound pressure extremes, the predicted curves from ST-TDIM show local numerical oscillations and amplitude deviations, while MST-TDIM suppresses these phenomena, with its predicted waveforms aligning more closely with the measured signals.

The local oscillations in the ST-TDIM predictions primarily arise from the simplified treatment of the monopole source component in the pure dipole model. Under the current operating conditions, since the monopole source strength contributes only a small portion, the prediction bias due to neglecting this component remains within an acceptable tolerance range, making the pure dipole model still highly applicable. The MST-TDIM incorporates the monopole mechanism into the sound field reconstruction framework, achieving more accurate and refined predictions while retaining the predictive capability of the pure dipole method.

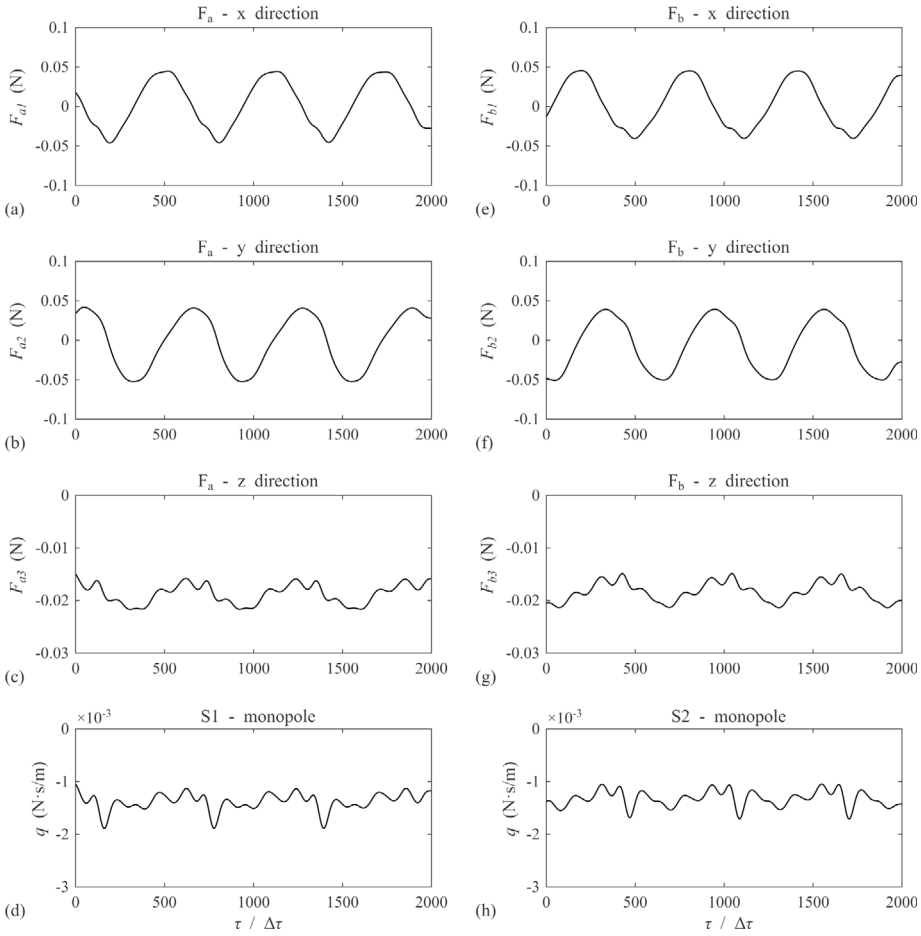

Fig. 16. Time-varying reconstruction of the UAV rotor source strength signals: (a) the x_1 direction components of the dipole source F_a; (b) the x_2 direction components of F_a; (c) the x_3 direction components of F_a; (e) the x_1 direction components of the dipole source F_b; (f) the x_2 direction components of F_b; (g) the x_3 direction components of F_b; (d) the monopole source Q_a; (h) the monopole source Q_b.

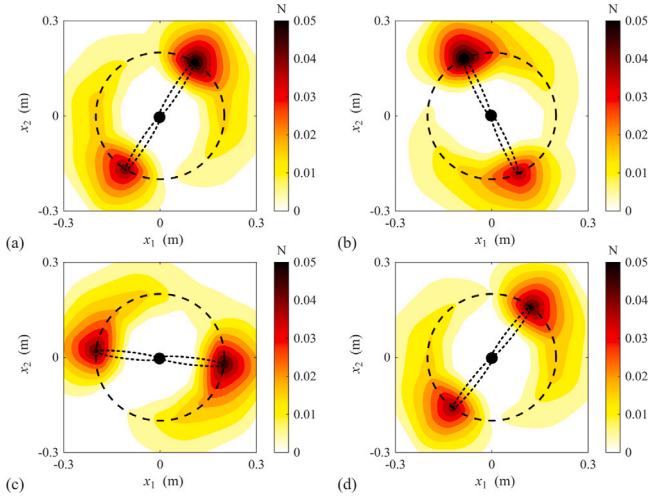

Fig. 17. The localization results of the two rotating blades (a) at time step τ_{100}; (b) at time step τ_{200}; (c) at time step τ_{300}; (d) at time step τ_{400}.

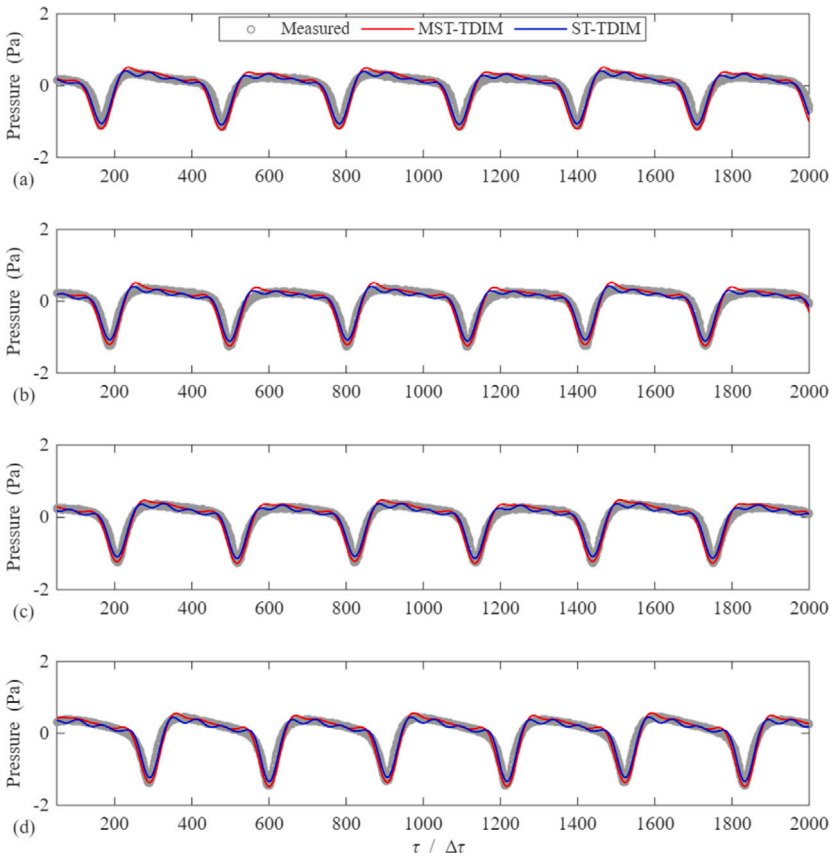

Fig. 18. Comparison of the predicted and measured pressures at four prediction points: (a) M1 (0.2, 0, 0.02) m; (b) M2 (0, 0.2, 0.02) m; (c) M3 (−0.2, 0, 0.02) m; (d) M4 (0, −0.2, 0.02) m.

5. Conclusion

This work introduces a novel time-domain inverse framework for identifying unsteady rotor noise sources, addressing the limitations of conventional frequency-domain approaches that assume steady or quasi-steady behaviour. The framework reconstructs unsteady rotating source strengths by combining the FW–H equation's integral solution under the assumption of neglecting the quadrupole noise source term with an equivalent source inversion method. The acoustic field is discretized via Eq. (17), linking source strengths to measured pressures through a transfer matrix in Eq. (39). To address ill-conditioning in the inverse problem of Eq. (41), a spatiotemporal regularization with mixed $\ell_{\alpha,\beta}$ norms from Eq. (42) is introduced, where $\alpha \leq 1$ promotes spatial sparsity for concentrated sources, and $\beta = 2$ ensures temporal continuity. The iterative solution in Eq. (49) leverages reweighted least squares with adaptive weights from Eqs. (46)–(47), initialized via Tikhonov regularization in Eq. (50) and terminates upon functional convergence in Eq. (52). The framework enables stable and accurate reconstruction of time-varying source strengths, offering a unified approach for source localization, temporal evolution tracking, and radiated sound field prediction, while retaining flexibility for diverse source distributions and robustness against noise.

Numerical simulations and experimental validation confirmed that the proposed time-domain method provides accurate localization and robust sound field prediction of rotor noise sources under a wide range of operating conditions. The method employed equivalent sources distributed on concentric rings with radii of 0.1 m to 0.3 m in simulations, reconstructed through the discretized formulation in Eq. (17). Results demonstrated accurate source localization and sound-field prediction across three rotational-speed cases at 1000, 3000, and 5000 rpm. In addition, a noise-robustness study was carried out by sweeping the SNR from 0 dB to 30 dB, where the phase evaluation factor E_p remained close to 1 and the amplitude evaluation factor E_a remained close to 0, indicating stable reconstruction in noisy environments. Furthermore, a geometric sensitivity study was performed by varying the number of equivalent sources and the measurement-to-equivalent-source-surface distance, showing that the proposed method maintains high reconstruction accuracy provided that the equivalent-source and measurement configurations are reasonably arranged. The implementation used a 12.8 kHz sampling rate, λ-regularized inversion from Eq. (48), and spatiotemporal weighting via Eq. (49) configured with $\alpha \leq 1$ and $\beta = 2$ norm parameters. Experimental validation was conducted using small UAV rotor at a rotational speed of 999 rpm. The method demonstrated accuracy in identifying rotor noise sources with prediction errors below 18 dB

under semi-anechoic chamber conditions, while effectively capturing the radiation patterns. The proposed method enables real-time localization of rotor noise sources and accurately reconstructs the time-varying history of the corresponding source intensity signals. Experimental results indicate that, under subsonic conditions, rotor noise sources primarily consist of dipole-type loading noise and monopole-type thickness noise. For thin blades such as those of small UAV rotors operating at low rotational speeds, the contribution of monopole-type thickness noise is relatively minor, while dipole-type loading noise becomes dominant. Moreover, the loading force signals exhibit harmonic behaviour characterized by sinusoidal patterns in the x and y directions of the Cartesian coordinate system, and appear as negative periodic time-varying signals in the z direction. Furthermore, based on the reconstructed source information, the radiated time-varying sound field of the rotor is further predicted, which is of great significance for advancing real-time control of rotor noise and accelerating the development of the low-altitude economy.

It is worth emphasizing that the proposed time-domain inverse framework is primarily developed for, and has been validated under subsonic rotating-source conditions. For the highest rotational speed investigated in this study, 5000 rpm, corresponding to approximately $M \approx 0.3$, the Doppler factor $(1 - M_R)$ remains numerically stable. However, as $M_R \to 1$, the denominator term $(1 - M_R)$ may significantly amplify the integrand, leading to severe numerical ill-conditioning and potential singularities. Based on additional high-rotational-speed simulations under the same numerical setup, we observed that pronounced singular behaviour and numerical divergence start to appear when the rotational Mach number increases to approximately $M \approx 0.82$. Therefore, within the current inverse framework, this value can be regarded as a practical Mach-number limit for the considered simulation setting, and the proposed method should not be directly extrapolated to transonic or supersonic regimes without further modifications.

Nevertheless, extending the time-domain inversion concept to the identification of supersonic rotating aerodynamic noise sources remains meaningful. Future work will focus on establishing an effective time-domain relationship applicable to higher Mach-number conditions, and on developing the required theoretical and numerical treatments, e.g., singularity-removal and robust algorithms for the multiple-root retarded-time problem, to enable reliable identification of high-speed rotating aerodynamic noise sources and to deepen the understanding of their generation and propagation mechanisms.

CRediT authorship contribution statement

Ying Xu: Writing – original draft, Visualization, Validation, Methodology, Investigation, Formal analysis. **Zhonghua Peng:** Writing – original draft, Visualization, Validation, Software, Formal analysis. **Damiano Casalino:** Writing – review & editing, Supervision, Conceptualization. **Xiaozheng Zhang:** Writing – original draft, Validation, Methodology, Investigation, Conceptualization. **Yunjin Tong:** Writing – original draft, Software, Formal analysis. **Chuanxing Bi:** Writing – review & editing, Supervision, Project administration, Funding acquisition. **Shiying Xiong:** Writing – review & editing, Supervision, Methodology, Funding acquisition, Conceptualization.

Declaration of competing interest

The authors declare that they have no known competing financial interests or personal relationships that could have appeared to influence the work reported in this paper.

Acknowledgements

The authors acknowledge support of the National Natural Science Foundation of China (grant nos. 12504544, 12574505, and 12302294), the Fundamental Research Funds for the Central Universities (grant no. PA2024GDSK0040), and the Academic Newcomer Advancement Program (Category A) of Hefei University of Technology (grant no. JZ2024HGTA0265).

Data availability

Data will be made available on request.

References

[1] D. Casalino, W. Velden, G. Romani, Community noise of urban air transportation vehicles, in: Proc. AIAA Aerosp. Sci. Meet., 2019, p. 1834.
[2] D. Casalino, W. Velden, G. Romani, I. Gonzalez-Martino, Aeroacoustic analysis of urban air operations using the LB/VLES method, in: Proc. 25th AIAA/CEAS Aeroacoustics Conf., 2019, p. 2662.
[3] Y. Fuerkaiti, D. Casalino, F. Avallone, D. Ragni, Aircraft community noise prediction in 3D environments using Gaussian beam tracing, in: Proc. 28th AIAA/CEAS Aeroacoustics Conf., 2022, p. 3079.
[4] K. Ekici, K.C. Hall, E.H. Dowell, Computationally fast harmonic balance methods for unsteady aerodynamic predictions of helicopter rotors, J. Comput. Phys. 227 (2008) 6206–6225.
[5] M. Carley, Load and thrust noise of rotors in forward flight, J. Fluid Mech. 552 (2006) 143–172.
[6] J. Christophe, S. Moreau, L. Brosset, Broadband noise modeling of wind turbines: Recent developments and applications, J. Sound Vib. 504 (2021) 116–125.
[7] C. Brehm, M.F. Barad, C.C. Kiris, Development of immersed boundary computational aeroacoustic prediction capabilities for open-rotor noise, J. Comput. Phys. 388 (2019) 690–716.
[8] C.R. Lowis, P.F. Joseph, Determining the strength of rotating broadband sources in ducts by inverse methods, J. Sound Vib. 295 (2006) 614–632.
[9] C.R. Lowis, S.J. Joseph, N.A. Berton, K.J. Ryan, G.J. Page, Estimation of the far-field directivity of broadband aeroengine fan noise using an in-duct axial microphone array, J. Sound Vib. 329 (2010) 3940–3957.

[10] W. Ma, H. Bao, C. Zhang, Y. Wang, M. Yang, Beamforming of phased microphone array for rotating sound source localization, J. Sound Vib. 467 (2020) 115064.
[11] W. Ma, C. Zhang, Doppler effect in the time-domain beamforming for rotating sound source identification, J. Acoust. Soc. Am. 148 (2020) 430–443.
[12] P.X. Mo, W.K. Jiang, A hybrid deconvolution approach to separate acoustic sources in multiple motion modes, J. Acoust. Soc. Am. 142 (2017) 276–285.
[13] O. Jaeckel, Strengths and weaknesses of calculating beamforming in the time domain, in: Proceedings of the 1st Berlin Beamforming Conference, BeBeC, Berlin, Germany, 2006, p. 2.
[14] P. Sijtsma, S. Oerlemans, H. Holthusen, Location of rotating sources by phased array measurements, in: Proc. 7th AIAA/CEAS Aeroacoustics Conf. Exhibit, 2001, p. 2167.
[15] P. Sijtsma, H. Holthusen, Source location by phased array measurements in closed wind tunnel test sections, in: 5th AIAA/CEAS Aeroacoustics Conference, 1999, p. 1814.
[16] S. Oerlemans, P. Sijtsma, B.M. Lopez, Location and quantification of noise sources on a wind turbine, J. Sound Vib. 299 (2007) 869–883.
[17] P. Sijtsma, Using phased array beamforming to identify broadband noise sources in a turbofan engine, Int. J. Aeroacoustics 9 (2010) 357–374.
[18] O. Minck, N. Binder, O. Cherrier, Fan noise analysis using a microphone array, in: International Conference on Fan Noise, 2012, pp. 1–9.
[19] N. Chu, H. Qian, Y. Liang, Rotating acoustic source localization: a power propagation forward model and its high-resolution inverse methods, Meas. 174 (2021) 109006.
[20] N. Chu, Q. Liu, L. Yu, High-resolution localization of rotating acoustic sources: An experimental investigation and axial fan application, Meas. 196 (2022) 111149.
[21] M. Debrouwere, D. Angland, Airy pattern approximation of a phased microphone array response to a rotating point source, J. Acoust. Soc. Am. 141 (2017) 1009–1018.
[22] X. Zhang, Z.G. Chu, Y. Yang, An alternative hybrid time- frequency domain approach for rotating acoustic source identification, IEEE Access 7 (2019) 59797–59805.
[23] R.P. Dougherty, B. Walker, Virtual rotating microphone imaging of broadband fan noise, in: 15th AIAA/CEAS Aeroacoustics Conference, 2009, p. 3121.
[24] G. Herold, C. Ocker, E. Sarradj, A comparison of microphone array methods for the characterization of rotating sound sources, in: 7th Berlin Beamforming Conference, 2018, p. 22.
[25] G. Herold, E. Sarradj, Microphone array method for the characterization of rotating sound sources in axial fans, Noise Control Eng. J. 63 (2015) 546–551.
[26] M. Kerscher, B. Vonrhein, F. Ueberle, How acoustic camera measurements can help to increase the acceptance of wind turbines, in: Wind Europe Summit, 2016.
[27] D. Casalino, G. Romani, R. Zhang, H. Chen, Lattice-Boltzmann calculations of rotor aeroacoustics in transitional boundary layer regime, Aerosp. Sci. Technol. 130 (2022) 107953.
[28] D. Casalino, G. Romani, L.M. Pi, R. Colombo, Flow - confinement effects on sUAS - rotor noise, Aerosp. Sci. Technol. 143 (2023) 108756.
[29] C. Bogey, C. Bailly, A family of low dispersive and low dissipative explicit schemes for flow and noise computations, J. Comput. Phys. 194 (2004) 194–214.
[30] R. Astley, R. Sugimoto, P. Mustafi, Computational aero-acoustics for fan duct propagation and radiation. current status and application to turbofan liner optimisation, J. Sound Vib. 330 (2011) 3832–3845.
[31] J.B. Keller, D. Givoli, Exact non-reflecting boundary conditions, J. Comput. Phys. 82 (1989) 172–192.
[32] J.-P. Berenger, A perfectly matched layer for the absorption of electromagnetic waves, J. Comput. Phys. 114 (1994) 185–200.
[33] F. Hu, M. Pizzo, D. Nark, On a time domain boundary integral equation formulation for acoustic scattering by rigid bodies in uniform mean flow, J. Acoust. Soc. Am. 142 (2017) 3624–3636.
[34] Z. Wang, S.W. Rienstra, C. Bi, B. Koren, An accurate and efficient computational method for time-domain aeroacoustic scattering, J. Comput. Phys. 412 (2020) 109442.
[35] C.X. Bi, Y. Xu, Y.B. Zhang, A time-domain inverse method for the localization and quantification of unsteady rotating loading sources, J. Sound Vib. 512 (2021) 116405.
[36] Y. Xu, X.Z. Zhang, D. Casalino, Spatial and temporal reconstruction of unsteady rotating forces through an inverse acoustic method, Mech. Syst. Signal Process. 200 (2023) 110596.
[37] Y. Xu, D. Casalino, X.Z. Zhang, C.X. Bi, Real-time reconstruction of unsteady rotating forces acting by rotor blades in moving medium, J. Sound Vib. 568 (2024) 117972.
[38] X.Z. Zhang, C.X. Bi, Y.B. Zhang, L. Xu, A time-domain inverse technique for the localization and quantification of rotating sound sources, Mech. Syst. Signal Process. 90 (2017) 15–29.
[39] M.J. Lighthill, On sound generated aerodynamically. I. General theory, Proc. R. Soc. Lond. A. 211 (1952) 564–587.
[40] D.L. Hawkings, M.V. Lowson, Theory of open supersonic rotor noise, J. Sound Vib. 36 (1974) 1–20.
[41] S.B. Pope, Turbulent Flows, Cambridge University Press, 2000.
[42] J.E.F. Williams, D.L. Hawkings, Sound generation by turbulence and surfaces in arbitrary motion, Philos. Trans. R. Soc. A 264 (1969) 321–342.
[43] S. Glegg, W. Devenport, Aeroacoustics of Low Mach Number Flows: Fundamentals, Analysis, and Measurement, Academic Press, London, 2017.
[44] C.R. Lowis, P.F. Joseph, Determining the strength of rotating broadband sources in ducts by inverse methods, J. Sound Vib. 295 (2006) 614–632.
[45] P.A. Nelson, S. Yoon, Estimation of acoustic source strength by inverse methods: Part I, conditioning of the inverse problem, J. Sound Vib. 233 (2000) 643–668.
[46] S.H. Yoon, P.A. Nelson, Estimation of acoustic source strength by inverse method: Part II, experimental investigation of methods for choosing regularization parameters, J. Sound Vib. 233 (2000) 669–705.
[47] D.P.O. Leary, P.C. Hansen, The use of the L-curve in the regularization of discrete ill-posed problems, SIAM J. Sci. Comput. 14 (6) (1993) 1487–1503.
[48] M. Aucejo, Structural source identification using a generalized tikhonov regularization, J. Sound Vib. 333 (2014) 5693–5707.
[49] M. Aucejo, O.D. Smet, Bayesian source identification using local priors, Mech. Syst. Signal Process. 66–67 (2016) 120–136.
[50] E.G. Williams, Regularization methods for near-field acoustical holography, J. Acoust. Soc. Am. 110 (2001) 1976–1988.
[51] B. Qiao, X. Zhang, J. Gao, Impact-force sparse reconstruction from highly incomplete and inaccurate measurements, J. Sound Vib. 376 (2016) 72–94.